Thesis for the Degree of Master of Engineering

Fabrication of APTMS Functionalized-Magnetite Nanoparticle and Controlling the Optimum Dose for Hyperthermia Cancer Therapy

by

Yosefine Arum

Department of Mechatronic

The Graduate School

Pukyong National University

August 2011

APTMS 기능화된 자기 나노입자의 제작과 온열 암 치료를 위한 최적화

Advisor: Prof. Oh Junghwan

by

Yosefine Arum

A thesis submitted in partial fulfillment of the requirements

for the degree of

Master of Engineering

in Department of Mechatronic, The Graduate School,

Pukyong National University

August 2011

Fabrication of APTMS Functionalized-Magnetite Nanoparticle and Controlling the Optimum Dose for Hyperthermia Cancer Therapy

A thesis

by

Yosefine Arum

Approved by

_____

(Chairman) In-Pil Kang

_____ _____

(Member) Jeong-Hyun Sohn (Member) Jung-Hwan Oh

June, 2011

TABLE OF CONTENTS

LIST OF FIGURES

LIST OF TABLES

Fabrication of APTMS functionalized-Magnetite Nanoparticle and Controlling the Optimum Dose for Hyperthermia Cancer Therapy

Yosefine Arum

Department Mechatronic, The Graduate School,

Pukyong National University

Abstract

Magnetic hyperthermia has been used for many years to treat a variety of malignant tumors. One of the problems in magnetic hyperthermia is the choice of the correct particle concentration in order to achieve a defined temperature increase in the tumor tissue. Using the correct nanoparticle dosage and considering their specific loss power, it is possible to estimate the efficiency of this therapeutic method.

In this study, we synthesized (3-Aminopropyl)-trimethoxysilane (APTMS)-functionalized Fe_3O_4 MNPs and evaluated magnetic heat distribution induced by these particles in agar tissue phantom when it subjected to the AC magnetic filed. By varying the concentration of particles, we determined the optimum dose to achieve a defined temperature of 42^oC or higher in the tumor tissue. The experimental data were compared with computer-based model, which was created using COMSOL Multiphysics to simulate the heat dissipation within the tissue for typical configurations of the tumor position as well as particle distribution within the tumor. In our findings, the simulation data were comparable to the actual experimental data and the heat dose of 19.9 W/g_{tissue} was acceptable for 5 mm tumor. Further, the cell study using HeLa cancer cell demonstrated that heating the cancer cells up to 50^oC for 10 min was sufficient for complete cell killing and cell viability assay showed that Fe_3O_4-APTMS MNPs exhibited no significant cytotoxicity against HeLa cells. Additionally, it was observed that the FITC-labeled Fe_3O_4-APTMS MNPs presented high cell biocompatibility and cellular uptake for efficient endocytosis.

Keyword: Hyperthermia, magnetic nanoparticles doses, SAR, tumor.

APTMS 기능화된 자기 나노입자의 제작과 온열 암 치료를 위한 최적화

Yosefine Arum

메카트로닉스 공학과
부경 대학교 대학원

초 록

자기 온열치료는 악성 종양의 치료방법의 한 형태로서 수 년간 다양한 종양의 치료에 사용되어왔다. 자기 온열치료의 문제점 중 하나는 종양 조직의 사멸온도로 정의된 온도의 도달을 위해 효율적인 나노입자 농도를 선택해야 한다는 것이다. 나노입자의 투여효율 및 자기 나노입자의 SLP(specific loss power)를 고려하면, 자기 온열치료 요법의 효율성을 추정할 수 있다.

본 연구에서, 우리는 Fe_3O_4 자기 나노입자의 기능화를 통해 (3-Aminopropyl)-trimethoxysilane(APTMS)를 합성하였다. 합성된 자기 나노입자를 이용하여 한천 조직 팬텀을 제작하였고, 한천 조직 팬텀에 교류 자기장을 적용해 나노입자의 열 발생 및 자기 열 분포를 평가하였다. 다양한 나노입자의 농도를 통해, 우리는 종양 조직의 사멸온도로 정의된 42°C 이상의 온도를 달성하기 위한 최적의 복용량을 결정하였다. 또한 COMSOL Multiphysics를 이용해 조직 팬텀내 종양의 위치뿐만 아니라, 나노입자 분포의 전형적인 구성을 위한 컴퓨터 시뮬레이션 모델링을 통해 실험 결과의 정확성을 비교하였다. 컴퓨터 시뮬레이션을 통해 도출된 연구 결과는 5mm 조직 팬텀을 이용한 실제 실험의 결과 19.9W/g_{tissue}의 SLP와 유사하였다. 도출된 실험결과를 HeLa 암 세포에 적용하여 10분만에 50°C까지 도달 하는 것을 확인하였다. 또한 세포 생존능력 평가를 통하여 Fe_3O_4-APTMS MNPs의 HeLa 세포에 대한 세포 적합성을 평가하였고, 그 결과 Fe_3O_4- APTMS MNPs의 높은 세포적합성과 효율적인 세포 흡수를 증명하였다.

키워드 : 자기 온열치료, 자기 나노입자의 복용, SLP, 종양.

Chapter 1

Introduction

In recent years, nanometer particles have drawn a great deal of interest from the biomedical research world. Nanoparticles with sizes less than 100 nm possess unique properties (such as high surface-volume ratios, high reactivities, etc.) compared to their bulk micron-structured counterparts due mainly to size effects and surface phenomena at the nanoscale [8]. Magnetic nanoparticles (MNPs) are particularly promising in several biomedical applications, such as: (a) cellular therapy involving cell labeling and targeting and as a tool for cell-biology research to separate and purify cell populations; [9-10] (b) tissue repair; [11-13] (c) targeted drug delivery; [14-16] (d) magnetic resonance imaging (MRI); [17-18] (e) hyperthermia for cancer treatment; [4, 19-21] etc.

Magnetic hyperthermia represents one of the focal points in the research for an effective cancer therapy due to the promising heating capabilities of ferromagnetic nanoparticles and the advances in the specific delivery of these particles to the tumor. The method consists of inducing apoptosis to the cancer cells by generating heat locally from ferromagnetic or ferrimagnetic nanoparticles which are irradiated with an alternating electromagnetic field. The concentration distribu- tion of injected magnetic nanoparticles in a tumor and its nearby tissue can be mapped through magnetic resonance imaging (MRI) to provide guidance for thermotherapy applications (Figure 1-1). Upon exposure under alternative magnetic field (AMF), MNPs can generate heat through oscillation of their magnetic moment [22]. According to the National Cancer Institute, hyperthermia cancer treatment kills cancerous cells by elevating their temperatures to the therapeutic temperature range, 42-45°C. Its use is based on the fact that tumor cells are more

sensitive to heat at these temperatures than normal tissue cells because tumor cells are already stressed by low oxygen, higher than normal acid concentrations, and insufficient nutrients, and are thus significantly less able to tolerate the added stress of heat [23-25]. This approach can destroy tumors with minimal damage to healthy tissues and, therefore, limit negative side effects. Currently, oncologists often use hyperthermia cancer treatment in combination with radiotherapy and chemotherapy. In addition to eliminating many cancerous cells, hyperthermia can make resistant cells more vulnerable to other treatments.

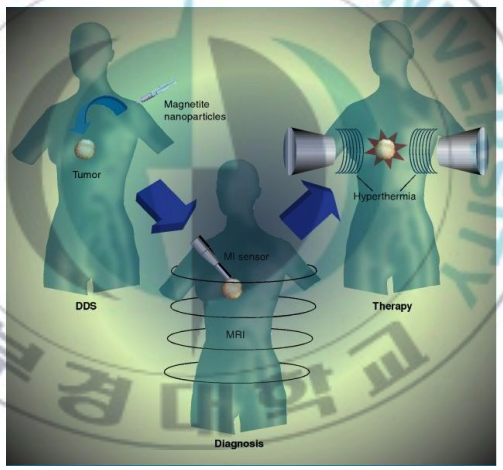

Figure 1-1. Scheme of magnetic hyperthermia therapy mediated by MNPs [1]

Magnetic fluid hyperthermia (MFH) cancer treatment involves injecting a fluid containing magnetic nanoparticles directly into tumors. For medical applications, the biocompatibility of both the fluid and nanoparticles must be considered. The fluid must have a neutral pH and physiological salinity. The particles should remain evenly dispersed throughout the fluid, and must therefore be small enough to avoid precipitation due to gravitational forces [7]. In addition, the magnetic material should not be toxic. For

this, the consideration of a generic magnetic biomedical nanoparticle is shown in Figure 1-2. The most commonly used materials are magnetite (Fe_3O_4) and maghemite (γ-Fe_2O_3), which due to their magnetic properties, low toxicity and good biocompatibility offer many efficient possibilities in biotechnology and medicine [22, 26-27]. In order to achieve these specific properties accurately, the particles must be uniform in all respects of their size, magnetic and coating characteristic. It is therefore crucial that synthesis method chosen can achieve a uniform formation of the required particles.

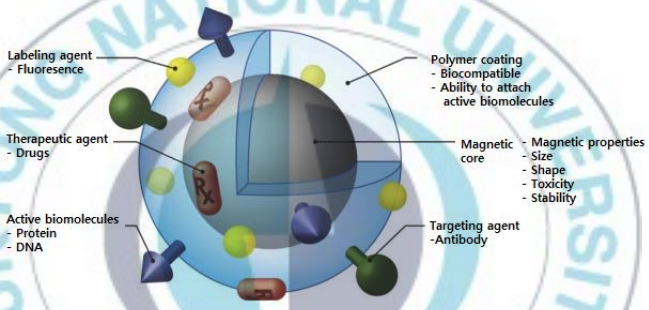

Figure 1-2. Generic design and considerations of biomedical magnetic nanoparticle [2]

A major challenge for hyperthermia is in minimizing the damage to the healthy tissue around the tumor through the creation of local hot spots. This requires careful temperature monitoring and manual interventions. These difficulties include the need to choose biocompatible values for field amplitude and frequency, the problem of quantifying the optimum dose of nanoparticles in order to limit the heating area to the tumor as precise as possible. The generated heat within the tissue can be attributed to three types of loss processes [26, 28] : hysteresis losses, which correspond to the ferromagnetic behavior of the particle, relaxation losses which account for most of the generated heat in the superparamagnetic regime, and resonance losses which would only

occur at high frequencies unsuitable for the MFH therapy and can thus be neglected [22], [29]. The efficiency of the transformation of energy is strongly dependent on the strength and frequency of the magnetic field and the properties of the magnetic particles [30]. While, tumors are classified as easy to heat or difficult to heat [31], depending upon their response to hyperthermia treatment. Malignant solid tumors that are characterized by specialized microenvironments, e.g., chaotic vasculature, low perfusion, acidosis, and hypoxia, are more sensitive to hyperthermia [32]. In these cases, the malignant tissue is more readily destroyed selectively while leaving normal tissue intact [33].

Several groups have investigated the spatial temperature distribution in a spherical region containing magnetic particles exposed to an AC magnetic field and compared in vitro experiments with mathematical simulations. Suto et al. [34] experimentally and numerically investigated the diffusion of a spherical heat source after dispersing magnetite nanoparticles in hydrogel. Recently, the use of magnetic sensitive agarose gel has been explored for hyperthermia applications [35-37]. However, the correct control of temperature has been a difficult and complicated challenge. The reason for these problem may be explained mainly by the insufficient administered heat dose against heat loss, resulting in the entire target cancer tumours not being heated up to tissue lethal temperature. The heat dose administered in tissue takes into account two factors: the heating power of magnetic material (W/g_{tissue}) that is represented by the specific absorption rate (SAR) [4], and the amount of magnetic nanoparticles accumulated in the cancer region, which is represented by the weight of particles per unit weight of target tumour tissue ($g_{material}/g_{tissue}$) [38]. The main issue that we have to address should be to set the objective heat dose values which overcome the amount of heat loss.

In this thesis, to address the issue above, we performed a systematical variation of

tumor diameter and particle dosage then observed the heat transfer process within the agar tissue by employing a computer-controlled heat simulator. Possibilities of achieving the estimated heat dose by integrating presently available technologies are discussed.

1.1. Motivation

The biological processes in cells, including cancer, are particularly susceptible to changes in temperature. In fact, a change in temperature of from 37 °C to 42 °C, is sufficient to kill a cancer cell provided the cell is exposed to this temperature for a sufficient period of time [39-40]. While the biology of thermal damage is well understood, this knowledge has translated poorly into clinical application for cancer therapy, although some success has been achieved for classic hyperthermia treatment [41-42]. One reason is the absence of technology that effectively localizes heat to the tumor without heating surrounding healthy tissues [43]. A second limitation is the inability to accurately measure the heat dose deposited into the tumor relative to surrounding tissue [32, 44].

One technology being developed to address these limitations is the activation of susceptor materials such as MNPs by excitation with an external alternating magnetic field. However, the lack of information on which characteristics are important for delivering the maximum heat dose per gram of injected material is a significant issue [45-46]. It is the objective of this study to address this issue; in particular, to identify one characteristic that is important for delivering the maximum heat dose per gram of injected material.

1.2. Specific Aims of this Study

For bio applications such as heating elements for hyperthermia, however, a superparamagnetic is also an attractive material. For this purpose, it is important to know the targeted value of MNP size, because the mean size control attaining desirable average composition and uniformity of Fe_3O_4 MNPs is still a big challenge. And until now there has not yet been clarified an effective and safe limit of the temperatures achieved during the hyperthermia treatment within the tissue.

1. This study consists of fabrication and characterization of Fe_3O_4 MNPs. Surface modification was done by applying APTMS to make particles suitable for biomedical application.
2. Quantify the optimum dose of magnetic material that injected into the tumor would lead to a therapeutic temperature of at least 42^{o}C and observe the heat distribution within the agar tissue phantom.
3. Create a computational model in COMSOL: Multiphysics in order to analyze the heat dissipation within the tumor tissue.

By achieving these goals this study will help to choice of the right dose of nanoparticles and the optimum applied field parameters in order to achieve the desired temperature within a specified region inside the body.

Chapter 2

Background Theories

2.1. Special Features of Magnetic Nanoparticles

The key issues dominate the magnetic properties of nanoparticles are finite-size effects and surface effects which give rise to various special features.

2.1.1. Finite-Size Effects

In large magnetic particles (ferromagnetic), it is well known that there is a multidomain structure, where its magnetic moments (spins) aligned by exchange forces and pointing to the very same direction. Regions of uniform magnetization are separated by domain walls, as summarized in Figure 2.1. On the other hand, if the dimensions of the material under consideration is reduced drastically, until a few nanometers (1 nanometer = 10^{-9} = 0.000000001 meter), these domain walls will be forced to shrink and coexist in a small volume, thus increasing the "repulsion" among them. This proximity (density) of domains when the material reaches dimensions at the nanometer scale, yields the domains to merge into a single one, creating what is known as a single-domain particle (superparamagnetic). The formation of the domain walls is a process driven by the balance between the magnetostatic energy (ΔE_{MS}), which increases proportionally to the volume of the materials and the domain-wall energy (Δ_{dw}), which increases proportionally to the interfacial area between domains.

The exact dimension at which a nanostructured material passes from single-to multi-domain depends on each material, and is known as Critical Size. If the particle is spherical, it is called in critical diameter. If the sample size is reduced, there is a critical volume below which it costs more energy to create a domain wall than to support the

external magnetostatic energy (stray field) of the single-domain state. This critical diameter typically lies in the range of a few tens of nanometers and depends on the material. It is influenced by the contribution from various anisotropy energy terms. The critical diameter of a spherical particle (D_c) below which it exists in a single-domain state is reached when $\Delta E_{MS} = \Delta_{dw}$, which implies, $D_c \approx 18\sqrt{\frac{A\kappa_{eff}}{\mu_0 M^2}}$, where A is the exchange constant, κ_{eff} is anisotropy constant, μ_0 is the vacuum permeability, and M is the saturation magnetization. Typical values of D_c for some important magnetic materials are listed in Table 2-1.

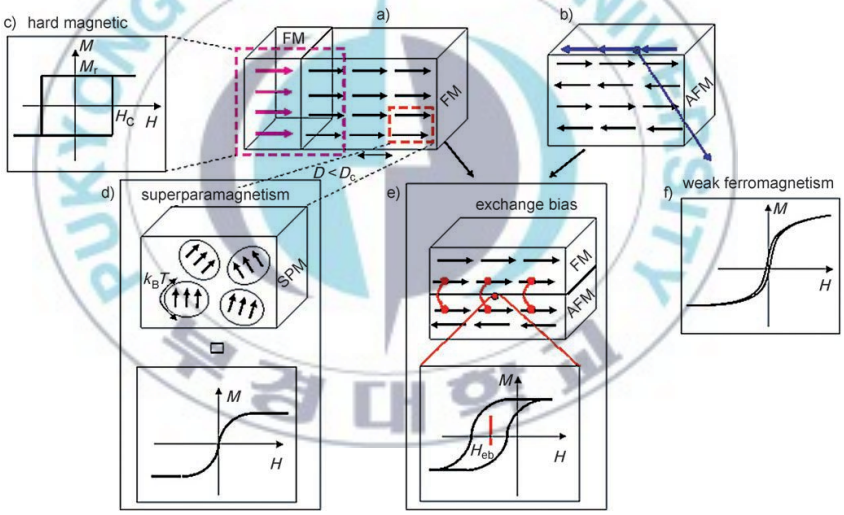

Figure 2-1. The different magnetic effects occurring in magnetic nanoparticles. The spin arrangement in (a) a ferromagnetic (FM) and (b) an antiferromagnetic (AFM), (c) the magnetization curve of ferromagnetic, (d) superparamagnetic (SPM) with single domain exhibit no remanence or coercivity, that is, there is no hysteresis in the magnetization curve, (e) the interaction (exchange coupling; linked red dots) at the interface between a ferromagnet and an antiferromagnet produces the exchange bias effect. In an exchange-biased system, the hysteresis is shifted along the field axis and the coercivity increases substantially, (f) pure antiferromagnetic nanoparticles could exhibit superparamagnetic relaxation as well as a net magnetization arising from uncompensated surface spins (blue arrows in (b))[47].

Table 2-1. Estimated single-domain size for different spherical particles [6].

Material	D_c (nm)
Hcp Co	15
Fcc Co	7
Fe	15
Ni	55
SmCo5	750
Fe_3O_4	128

A single-domain particle is uniformly magnetized with all the spins aligned in the same direction. The magnetization will be reversed by spin rotation since there are no domain walls to move. This is the reason for the very high coercivity observed in small nanoparticles [48]. Another source for the high coercivity in a system of small particles is the shape anisotropy. It must be remembered that the estimation of the critical diameter holds only for spherical and non-interacting particles. Particles with large shape anisotropy lead to larger critical diameters.

The second important phenomenon which takes place in nanoscale magnetic particles is the superparamagnetic limit. The superparamagnetism can be understood by considering the behavior of a well-isolated single-domain particle. The magnetic anisotropy energy per particle which is responsible for holding the magnetic moments along a certain direction can be expressed as follows: $E(\theta) = \kappa_{eff} V \sin^2\theta$, where V is the particle volume, κ_{eff} anisotropy constant and θ is the angle between the magnetization and the easy axis. The energy barrier $\kappa_{eff} V$ separates the two energetically equivalent easy directions of magnetization. With decreasing particle size, the thermal energy, $k_B T$, exceeds the energy barrier $\kappa_{eff} V$ and the magnetization is easily flipped. For $kT > \kappa_{eff} V$ the system behaves like a paramagnet, instead of atomic magnetic moments, there is now a giant moment inside each particle (Figure 2-1d). Such a system has no hysteresis and the data of different temperatures superimpose onto a universal curve of M versus H.

2.1.2. Surface Effect

As the particles size decreases, a large percentage of all the atoms in a nanoparticle are surface atoms, which implies that surface and interface effects become more important. Surface effects can lead to a decrease of the magnetization of small particles, for instance oxide nanoparticles, with respect to the bulk value. This reduction has been associated with different mechanisms, such as the existence of a magnetically dead layer on the particles surface, the existence of canted spins, or the existence of a spin-glass-like behavior of the surface spins [49].

For magnetically inert surface coatings, organic ligands which used to stabilize the magnetic nanoparticles have an influence on their magnetic properties. They can modify the anisotropy and magnetic moment of the metal atoms located at the surface of the particles. As Paulus and co-workers reported, cobalt colloidal particles stabilized with organic ligands show a reduction of the magnetic moment and a large anisotropy [50]. Moreover, Leeuwen et al. proposed that surface-bonded ligands lead to the quenching of the surface magnetic moments, resulting in the reduction of magnetization [51].

In contrast, a magnetic coating on a magnetic nanoparticle usually has a dramatic influence on the magnetic properties. The combination of two different magnetic phases will lead to new magnetic nanocomposites. Metallic particles embedded in a matrix are interesting systems of magnetic-coated particles. Skumryev et al. have demonstrated the role of the matrix in establishing the magnetic response of small particles [52]. The magnetic behavior of the isolated 4-nm Co particles with a CoO shell changes dramatically when, instead of being embedded in a paramagnetic matrix, they are embedded in an antiferromagnetic matrix. The blocking temperature of Co particles embedded in an Al_2O_3 or C matrix was around 10 K, but by putting them in a CoO matrix,

they remain ferromagnetic up to 290 K. Thus, the coupling of the ferromagnetic particles with an antiferromagnetic matrix is a source of a large additional anisotropy.

2.2. Synthesis and Surface Modification of Magnetic Nanoparticles

For more effective therapeutic treatments, materials with highly saturated magnetization (such as transition metals (e.g. Fe, Co, Ni) or metal oxides (e.g. Fe_3O_4, γ-Fe_2O_3)) are usually considered. Although pure metals possess the highest saturation magnetization, they are highly toxic and extremely sensitive to oxidation [53], therefore, without a further appropriate surface treatment such pure metal nanoparticles are not relevant for biomedical applications [54-56]. In contrast, iron oxides are less sensitive to oxidation and, therefore, can give a stable magnetic response. In fact, small iron oxide nanoparticles have been applied to in vitro diagnosis for about 50 years [57]. Iron oxide magnetic nanoparticles can be prepared by several different methods including co-precipitation, thermal decomposition, micelle synthesis, and hydrothermal synthesis. A brief summary is shown in Table 2-2 [58].

Table 2-2. Summary comparison of various magnetic nanoparticle synthesis methods.

Synthesis method	Synthesis	Reaction temp [59]	Reaction period	Solvent	Size distribution	Shape control
Co-precipitation	Very simple, ambient conditions	20-90	Minutes	water	Relatively narrow	Not good
Thermal decomposition	Complicated, inert atmosphere	100-320	Hours-day	Organic compound	Very narrow	Very good
Microemulsion	Complicated, ambient condition	20-50	Hours	Organic compound	Relatively narrow	Low
Hydrothermal synthesis	Simple, high pressure	220	Hours-day	Water-ethanol	Very narrow	Very good

In terms of simplicity of the synthesis, co-precipitation is the preferred route. In terms of size and morphology control of the nanoparticles, thermal decomposition seems the best method developed to date. As an alternative, microemulsions can also be used to synthesize monodispersed nanoparticles with various morphologies. However, this method requires a large amount of solvent. Hydrothermal synthesis is a relatively little explored method for the synthesis of magnetic nanoparticles, although it allows the synthesis of high-quality nanoparticles. To date, magnetic nanoparticles prepared from co-precipitation and thermal decomposition are the best studied, and they can be prepared on a large scale.

To achieve monodispersity, these two stages must be separated and nucleation should be avoided during the period of growth. This is the classical model proposed by LaMer and Dinegar [60] first to explain the mechanism of formation of sulfur colloids and also for a limited number of cases (curve I of Figure 2-2). However, uniform particles have also been obtained after multiple nucleation events. The uniformity of the final product is in this case achieved through a self-sharpening growth process (Ostwald ripening, curve III of Figure 2-2) [61].

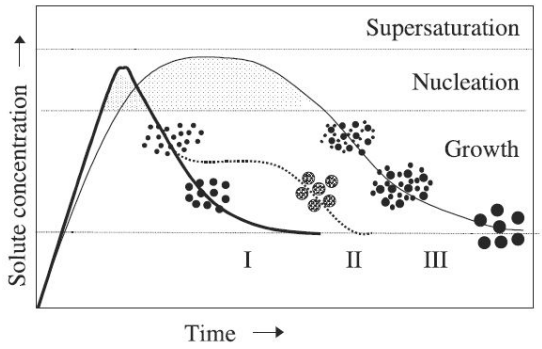

Figure 2-2. Mechanism of formation of uniform particles in solution: curve I: single nucleation and uniform growth by diffusion (classical model of LaMer and Dinegar); curve II: nucleation, growth and aggregation of smaller subunits; curve III: multiple nucleation events and Ostwald ripening growth [7].

In addition, uniform particles have also been obtained as a result of aggregation of much smaller subunits rather than continuous growth by diffusion (curve II of Figure 2-2) [62]. An artificial separation between nucleation and growth processes may be achieved by seeding in which foreign particles are introduced into the solution of monomers below the critical supersaturation [63].

However, biomedical applications are required hydrophilic particles. Thus surface modification should be done by applying hydrophilic polymers. Some of the strategies followed to achieve this are described and are summarized in Table 2-3. Several methods have been proposed to increase the suspension stability since magnetic nanoparticles are ready to form aggregates due to attractive van der Waals or magnetic dipole–dipole interactions, and their stability can change with pH values and salt concentrations under physiological conditions. Therefore, stability of magnetic nanoparticles under biological conditions is one of the important parameters to consider for biological applications.

Table 2-3. Routes for transferring to water hydrophobic magnetic nanoparticles prepared by thermal decomposition of organic precursor [7].

Coating	**Method**	**Examples**
Bifunctional molecules	Ligan exchange	DMSA [64-65] , Citric acid [66], Phosphonates [67], MAOH [68].
	Oleic acid Oxidation	O_3 [69], KMnO4 [70]
Polymers	Intercalation	Pluronic F-127 [71-72], Cyclodextrines [73]
	Ligand exchange	PAA-PAH [74] , PNIPAAm-b-PNIPPAAm [75] , HOOC-PEG- COOH [76]
	Polymerization on the particles	2-bromopropionylester [77]
Silica	Sol/gel	TEOS [78]
	Ligand exchange	APTMS [47]
	Reverse micells	Silsesquioxane [79], Triton X-100/Hexanol [80]
Gold	Heterogeneous nucleation	Au on Fe_3O_4: $Au(acet)_2$ [81-82]
	Bifunctional bridge molecule	Fe_3O_4 on Au: $Fe(CO)_5$ [83]

2.3. Heating Magnetic Nanoparticles with Alternating Magnetic Field

There are essentially two different mechanisms of heating experienced by the nanoparticle in the presence of an alternating magnetic field. Both mechanism exist in both magnetic and non-magnetic nanoparticles – the extent of heating is only difference. Eddy current heating is negligible in small sized particles.

2.3.1. Power Dissipation in Non-magnetic Nanoparticles

Faraday's law of induction suggests that a change in the magnetic flux generates an electric field and in effect a flow of current in a conductive medium. The resistance to this induced current [84] generates the power loss due to heat.

$$\nabla \times E = -\frac{dB}{dt} \tag{2.1}$$

Farady's law with E as the electric field and B as the magnetic flux density.

The remaining Maxwell's equations help to drive the power lost as heat in the presence of magnetic field.

$$\nabla \times H = J + \frac{dD}{dt} \tag{2.2}$$

Ampere's law with H as magnetic field density, J as the current density and D as the electric flux density [3, 85]

$$\nabla \cdot B = 0 \tag{2.3}$$

Gauss's law for magnetism with B as the magnetic flux density [3, 85]

$$\nabla \cdot D = \rho \tag{2.4}$$

Gauss's law for electricity with D as the electric flux density [3, 85]

Equations for power conservation can be derived from Maxwell's equations [86]. This is as follow.

$$\nabla \cdot (E \times H) = H \cdot (\nabla \times E) - E \cdot (\nabla \times H) \tag{2.5}$$

$$\nabla \cdot (E \times H) = H \cdot (-\frac{dB}{dt}) - E \cdot (J + \frac{dD}{dt}) \tag{2.6}$$

$$\nabla \cdot (E \times H) + \frac{d}{dt}\left(\frac{1}{2}\mu H^2 + \frac{1}{2}\varepsilon E^2\right) + E \cdot J = 0 \tag{2.7}$$

The final equation expresses the most general energy conservation situation. In that, when energy is supplied to coil (*E.J* term), it is converted into an electromagnetic wave and a magnetic field (The *E.J* term includes the resistive losses the coil). It is this magnetic field and electromagnetic wave generated that the nanoparticles get exposed to. Therefore, the sum of the energy density of an electromagnetic wave $\nabla \cdot (E \times H)$ and the energy stored in an electric field and magnetic field $-\frac{d}{dt}\left(\frac{1}{2}\mu H^2 + \frac{1}{2}\varepsilon E^2\right)$ should equal to the loss generated (*E.J* term) by the nanoparticle with a conductivity σ, dielectric constant of ε and magnetic permeability of μ.

The power generated due to eddy current loss can then be determined by taking the volume integral of the square of spatial change in magnetic field strength density (assuming quasistatic approximation for the nanoparticles) divided by the conductivity of the nanoparticle.

$$P = \int \frac{J^2}{\sigma} dV = \int \frac{(\nabla \times H)^2}{\sigma} dV \text{ [3, 87]} \tag{2.8}$$

Faraday's law suggested that a temporal change was only necessary in generating a current, but the spatial change in magnetic field strength determines the magnitude of the current. The depth from the surface of the particle necessary to drop the magnetic field strength to e^{-1} of its strength at the surface is known as the skin depth. The *skin depth* of a highly conductive material ($\sigma >> \omega\varepsilon$) is given by the following equation [3, 85].

$$d_p = \sqrt{\frac{2}{\omega\mu\sigma}} \tag{2.9}$$

In order to obtain appreciable heating, the frequency of operation should be fairly large to allow for a small skin depth. Typically, the skin depth should be less than half the depth of the penetrating object [88-89].

2.3.2. Power Dissipation in Magnetic Nanoparticles

The first law of thermodynamics suggests that the internal energy for a system of constant density and unit volume (U) is equal to the sum of the heat added (Q) and the work done on the system (W) [90].

$$\delta U = \delta Q + \delta W \tag{2.10}$$

Assuming that no heat is added to the magnetic nanaoparticle $\delta Q = 0$ and the only work done is that by the magnetic field ($\delta W = H \,.\, dB$). The final result is then

$$\delta U = H \,.\, dB \text{ [90]} \tag{2.11}$$

H is the magnetic field intensity vector (A m^{-1}), B is the magnetic flux density vector (T). The applied magnetic field intensity and the resulting magnetic flux density occur in the same direction, reducing Eq. (2.11) to

$$\delta U = H \,.\, \delta B \text{ [90]} \tag{2.12}$$

where H and B are magnitudes.

The general equation for the magetic flux density B is

$$B = \mu_0(H+M) \text{ [3, 85]} \tag{2.13}$$

where μ_0 is the magnetic permeability of free space ($4\pi \times 10^{-7}$) and M (A m^{-1}) is the material constant for magnetization and is a function of the applied field

$$M = \chi H \text{ [3, 85]} \tag{2.14}$$

where χ is the magnetic susceptibility of the material.

Substituting Eq. (2.13) into Eq. (1.11) and solving for the cyclical increase in internal energy gives

$$\Delta U = -\mu_0 \oint M \, dH \tag{2.15}$$

This equation suggests that magnetic work is converted to internal energy if magnetization lags the applied field. To determine the amount the magnetization lags the applied field requires defining χ as a complex number

$$\chi = \chi' - i\chi'' \quad [90] \tag{2.16}$$

If the applied magnetic field is sinusoidal, it can be expressed in the Euler's form

$$H(t) = Re[\, H_0 e^{i\omega t} \,] = H_0 \cos(\omega t) \tag{2.17}$$

and the magnetization constant M then becomes

$$M(t) = Re[\, \chi H_0 e^{i\omega t} \,] = H_0 [\, \chi' \cos(\omega t) + \chi'' \sin(\omega t) \,] \tag{2.18}$$

Substituting Eq. (2.18) in Eq. (2.15) causes the in-phase component (χ' term) to vanish leaving only the out-of-phase component (χ'' term) of χ.

$$\Delta U = 2\mu_0 H_0^2 \chi'' \int_0^{2\pi/\omega} \sin^2 \omega t \, dt \tag{2.19}$$

Eq(2.19). gives the energy converted in one cycle and has to be multiplied by the frequency to get the overall volumetric power dissipation.

$$P = f\Delta U = \mu_0 \pi \chi'' f H_0^2 \tag{2.20}$$

With the help of Shliomis's [91], relaxation equation for a motionless magnetic fluid in an alternating field the χ'' term can be related to macroscopic material parameters. In his relaxation equation (Eq. (2.21)) M_0 is given *as* $M_0 = \chi_0 H_0 \cos \omega t$ where χ_0 is the macroscopic equilibrium susceptibility.

$$\frac{\delta M(t)}{\delta t} = \frac{1}{\tau}(M_0(t) - M(t)) \tag{2.21}$$

where τ is the relaxation time of the fluid.

Substituting Eq. (2.18) as M(t) and $M_0 = \chi_0 H_0 \cos \omega t$ into Eq. (2.21) gives

$$\chi = \frac{\chi_0}{1 + i\omega t} = \frac{\chi_0}{1 + (\omega\tau^2)} + i\frac{\omega\tau}{1 + \omega\tau^2}\chi_0 \tag{2.22}$$

Therefore $\chi'' = \frac{\omega\tau}{1+\omega\tau^2}\chi_0$ and can be substituted into Eq. (2.20) to give

$$P = \pi\mu_0\chi_0 H_0^2 f \frac{\omega\tau}{1+\omega\tau} \text{ [90]} \tag{2.23}$$

The equilibrium susceptibility χ_0 is assumed to be the chord susceptibility corresponding to Langevin equation, and expressed as

$$\chi_0 = \chi_i \frac{3}{\xi}\left(\coth\xi - \frac{1}{\xi}\right) \text{ [92]} \tag{2.24}$$

where $\xi = \mu_0 M_d H V_M / kT$; $M_s = \phi M_d$; $H = H_0 \cos 2\pi f t$; and ϕ is the volume fraction of MNPs. Here, M_d and M_s and are the domain and saturation magnetization, respectively. The initial susceptibility is given by $\chi_i = \mu_0 \phi M_d^2 V_M / 3kT$. The temperature rise is calculated as $\Delta T = P\Delta t / \rho c_p$ where ρ and c_p are the effective density and the effective specific heat.

There are two types of relaxation process that the ferrofluid experiences.

1. Brownian Relaxation - occurs when the magnetic moment is locked in the crystal axis of the particle, requiring that the particle rotate to align the magnetic moment with the applied field [90].

$$\tau_b = \frac{3\eta V_H}{kT} \tag{2.25}$$

where, η is the viscosity coefficient of the fluid, k is the Boltzman constant (1.38×10^{-23} J K^{-1}), T is absolute temperature (K), and V_H is hydrodynamic volume of the

particle = $\frac{\pi(D+2\delta)^3}{6}$

2. Néel Relaxation – at the higher frequency Brownian motion ceases and second mechanism (Néel Relaxation) starts to dominate where the magnetic moment within the particle rotates with the applied field [92].

$$\tau_N = \frac{\sqrt{\pi}}{2}\tau_0 \frac{exp\,\Gamma}{\Gamma^{1/2}} \tag{2.26}$$

$$\Gamma = \kappa \frac{4\pi R^3}{3kT} \tag{2.27}$$

where, κ is anisotropy constant.

A typical ferrofluid can have Brownian and Néel processes going on in parallel, as a result an effective relaxation time can be determined as follows [92]

$$\frac{1}{\tau} = \frac{1}{\tau_b} + \frac{1}{\tau_N} \tag{2.28}$$

and the resulting relaxation constant τ plugged back into Eq. (2.23) to obtain accurate power dissipation values.

2.3.3. Magnetic Hysteresis

Hysteresis is well known in ferromagnetic materials. It involves ferromagnetic material absorbing some portion of an external magnetic field such that when the external field is removed the material remains magnetized. It represents an energy cost for the magnetic dipoles that are 'lagging' with respect to the applied field. In such material the relationship between magnetic strength (H) and magnetic flux density (B) is not linier. A plot of B against H gives a curve that flattens out with further increase in magnetic field strength.

The point where the magnetic field strength results in no further change in flux

density is called magnetic saturation (M_s). When H is reduced to zero, at this point, it can be seen that some magnetic flux remains in the material even though the magnetizing force is zero. This is referred to as the point of retentivity (M_r) on the graph and indicates the remanence or level of residual magnetism in the material (some of the magnetic domains remain aligned but some have lost their alignment). As the magnetizing force is reversed, where the flux has been reduced to zero, this is called the point of coercivity ($-H_c$) on the curve. The reversed magnetizing force has flipped enough of the domains so that the net flux within the material is zero. The force required to remove the residual magnetism from the material is called the coercive force or coercivity of the material [27]. As the magnetizing force is increased in the negative direction, the material will again become magnetically saturated but in the opposite direction (point $-M_s$). Reducing H to zero brings the curve to point "$-M_r$". It will have a level of residual magnetism equal to that achieved in the other direction. Increasing H back in the positive direction will return B to zero. Notice that the curve did not return to the origin of the graph because some force is required to remove the residual magnetism. The curve will take a different path from point "H_c" back to the saturation point where it with complete the loop.

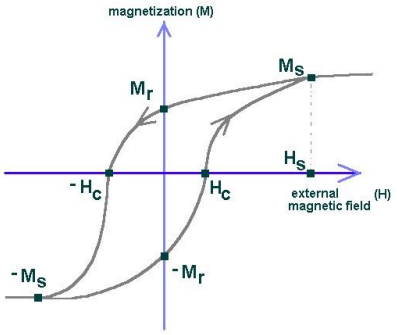

Figure 2-3. Hysteresis in ferromagnetic materials [3]

Plotting this relationship for all magnetic field strength in S shaped loops similar to Figure 2-3. The area of the middle bit of the S represents the work done on the system and represents the heat generated by ferromagnetic nanoparticles in the presence of an external magnetic field.

2.4. Specific Absorption Rate (SAR)

Specific absorption rate is a method to quantify the mass-normalized rate of RF energy absorption in human tissue. It is commonly adopted in bioelectromagnetics research as a menthod to quantify the rate of electromagnetic energy deposition in tissue, primarly in *in vitro* magetic hyperthermia studies. In such studies, SAR (W kg^{-1}) quantifies the amount of energy converted by the magnetic nanoparticle in the presence of the magnetic field. This is usually determined from time-dependent calorimetric measurements that measure the rate of temperature rise after applying the magnetic field (as seen in Figure 2-5). The typical experiment setup used to measure SAR (Figure 2-4) typically consists of a sample holder (this is well insulated) placed in the center of a coil while recording temperature change with a temperature probe. Typical temperature profiles are similar to that of Figure 2-4 with an initial temperature rise till thermal equilibrium is reached (flat part of curve). This is followed by an exponential decay in temperature as soon as the magnetic field is turned off.

Due to the fact that SAR is measured as the initial temperature rise it can be mathematically expressed as

$$SAR = c\frac{dT}{dt} \tag{2.29}$$

where c is specific heat and dT/dt is initial rate of temperature rise with respect to time.

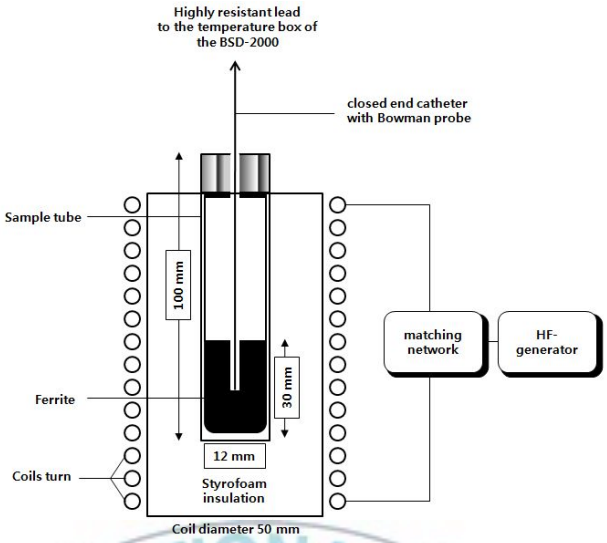

Figure 2-4. Experimental setup for SAR measurement [4]

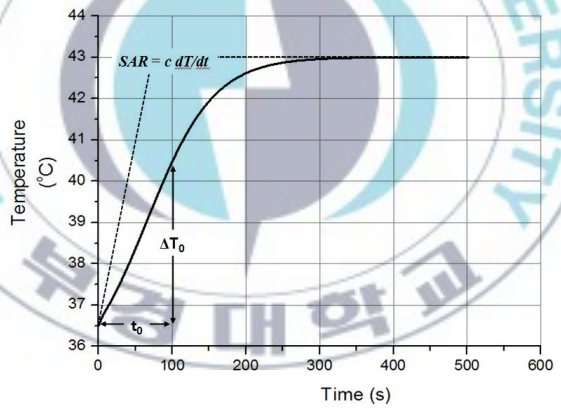

Figure 2-5. Typical temperature profile for SAR measurements [5]

The density of absorbed power is related to the SAR by

$$P = SAR\frac{m}{v} \tag{2.30}$$

The previous section described the various methods by which the magnetic particle generates heat. These mechanisms depend on frequency f, magnetic field strength H and material dependent constant κ. SAR should also have a form that describes dependency

on such parameters. Empirically SAR is found to be [26]

$$SAR \cong k f^n H^2 \tag{2.31}$$

where k is a frequency-dependent material constant incorporating κ and other parameters. Jordan, A. et al. along with other researchers [4, 26, 93] have reported in agreement that the empirical value of n ranges from 1.1 to 1.5. Although these are empirical results they are based in theory since Eq. (2.23) and Eq. (2.30) are of the same form (where k clumps up many of the terms). Therefore it is only reasonable to think of nanoparticle heating term of power delivered and not independent terms of frequency and magnetic field strength.

Chapter 3

Experimental Setup

Based on the design criteria described in chapter 2, we set out to synthesize monodisperse Fe_3O_4 MNPs via thermal decomposition method. Then surface of Fe_3O_4 MNPs were modified by functionalizing (3-Aminopropyl)-trimethoxysilane (APTMS) to make the magnetic nanoparticles become water soluble. Hyperthermia experimental observation was carried out by exposing Fe_3O_4-APTMS MNPs dispersed agar gel in an AC magnetic field with strength and frequency of 130 Oe and 154 kHz, respectively. The temperature distribution observed at the upper surface of agar tissue and compared the results with the theoretical estimation and computer simulation using COMSOL Multiphysics. In order to investigate the heat effect to the cell, HeLa cells were heated at certain temperature and the cell viability was observed. The cytotoxic effect of Fe_3O_4-APTMS MNPs was accomplished through the WST-1 assay and the cell uptake was verified by fluorescence cell labeling.

3.1. Synthesis of Magnetic Nanoparticles

The synthesis of Fe_3O_4 NPs were performed following the procedure reported by Park *et al.* [94]. The Fe-oleate complex was prepared by reacting 10.8 g of Fe(III) ($FeCl_3 \cdot 6H_2O$, 98%) and 36.5 g of sodium oleate (95%) were dissolved in a mixture solvent of 80 ml ethanol, 60 ml distilled water and 140 ml hexane. The resulting solution was heated to 70 °C for four hours. The two layers were observed, the upper organic layer containing the iron–oleate complex was washed three times with 30 ml distilled water in a separatory funnel. After washing, hexane was evaporated using rotary evaporator, then

oven under vacuum for 24 h resulting Fe-oleate complex in waxy solid. The next procedure is synthesis of monodisperse Fe_3O_4 NPs with a particle size of 14 nm. 36 g of the iron-oleate complex (resulted above) and 6.4 ml of oleic acid, 90% were dissolved in 253.8 ml of 1-octadecene, 90% (degassing octadecene previously at 120°C for 1 h). The reaction mixture was heated to 320 °C with a constant heating rate of 3.3 °C min^{-1}, and then kept at that temperature for 30 min. The resulting solution containing nanoparticles then washed with ethanol by centrifugation.

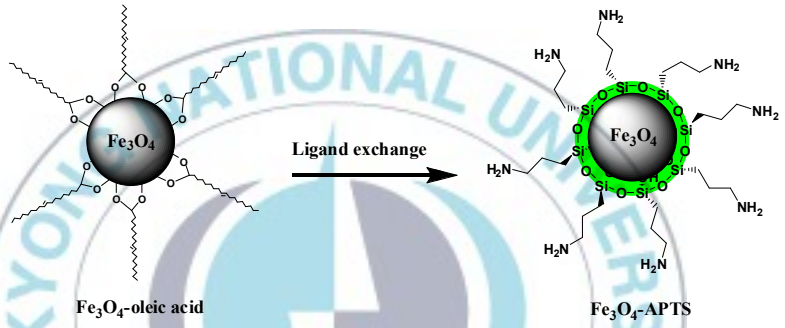

Figure 3-1. Synthesis route for Fe_3O_4-APTMS MNPs. The Fe_3O_4 -oleic acid was synthesized via thermal decomposition method. Then, oleic acid ligands were exchanged with APTMS, particles became water dispersible.

Water soluble Fe_3O_4 NPs were prepared by two-step silanization process by De Palma *et al.* [95], with little modification. 500 mg Fe_3O_4-oleic acid NPs were dispersed in 100 ml toluene and placed in three neck flask. Subsequently, 5 ml (3-Aminopropyl)-trimethoxysilane (APTMS) and 5 ml tetramethylammonium hydroxide (TMAH) 1 M were added and stirred under inert gas at 60°C for one hour. Precipitations were washed with toluene/methanol (1:1), solvent was removed under vacuum. In the second step, the solid precipitates were dissolved in 100 ml mixture of toluene/ethanol (4:1) and added with 5 ml TMAH 1 M stirred and heated to 60°C under inert gas for 1 hour. The solid precipitations were washed with the same procedure in step one. Finally, the colloidal

solution was dried under vacuum oven at 70°C for 3 h. The reaction schematic is presented in Figure 3-1.

3.2. Characterization of nanoparticles

The crystalline structure of Fe_3O_4 NPs examined with X-ray diffraction (XRD). The changes in the chemical groups were monitored using Fourier Transform Infra Red (FT-IR) spectrometer (JASCO FT/IR 4100, USA). Particle size was measured using Transmission Electron Microscopy (TEM) (JEOL, JEM-2010, Japan). Magnetic properties were measured using SQUID (Quantum Design, MPMS XL 7.0, USA).

3.3. Magnetic Heating Experiment

To verify the responsive of heat generated by Fe_3O_4-APTMS MNPs, we used a three turns coil (diameter 45 mm) which was powered with an induction heating system (7.5 kW WI-840, DIK, Korea) generating magnetic field (1.12×10^4 A/m, 154 kHz). 3 ml Fe_3O_4-APTMS MNPs with four different concentrations of 10, 12, 15 and 17 mg/ml were placed in 35 mm cell culture dish, thereafter particles were concentrated in the middle of dish by applying permanent magnet. After removing water, 3 ml agarose gel (1.2%) was added to each dish. Samples were subjected in the middle of coil and temperatures of the agar tissue at upper surface 5 mm away from the center of the MNPs was observed using infrared thermal imaging camera (FLIR System, USA) for 20 minutes. In order to investigate heat distribution in agar tissue, the results were compared by heating sample without agar tissue.

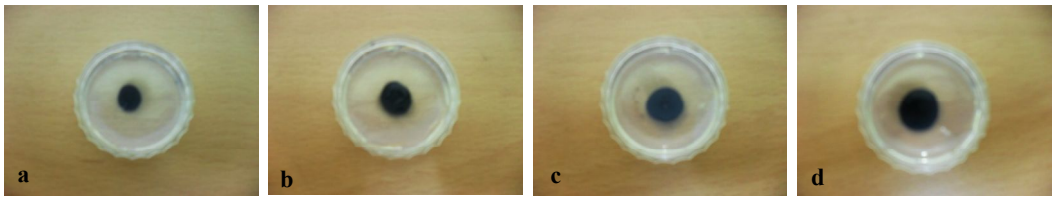

Figure 3-2. Experimental specimen (spherical heat source Fe_3O_4-APTMS MNPs, covered with agar gel) with concentrations (a) 10 mg/ml, (b) 12 mg/ml, (c) 15 mg/ml, and (d) 17 mg/ml.

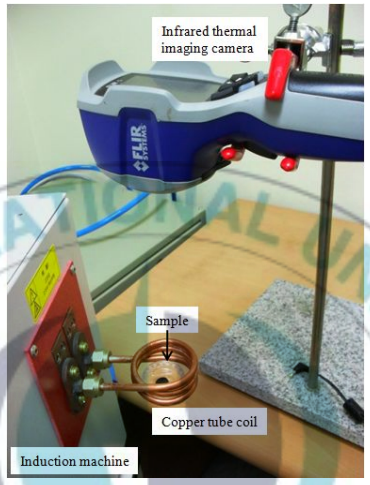

Figure 3-3. Induction of sample in agar gel.

3.4. **Measurement of heating potential of Fe_3O_4-APTMS represented by SAR**

The magnitude of the specific absorption rate (SAR) represents the heating power of particles and defined according to [96] as

$$SAR\,[Wg^{-1}(Fe_3O_4 - APTMS)] = \frac{C_{gel}}{x}\frac{dT}{dt} \tag{3.1}$$

where the specific heat of agarose gel C_{gel} is assumed to be equal to the specific heat of water, i.e. 4.18 J/g.C^o and dT (^{o}C)/dt (s) is the initial 30 s slope of the temperature versus time curve x is the weight fraction of magnetic elements in gel according to the formula

$$x = \frac{m(sample\,Fe_3O_4 - APTMS)}{m(H_2O) + m(agarose)} \tag{3.2}$$

where m are the masses of Fe_3O_4-APTMS, H_2O and agarose, respectively.

3.5. Cell Culture

HeLa cells (ATCC CCL-2) cultured in monolayer culture in Dulbecco's modified Eagle medium (DMEM, Thermo Scientific, USA) supplemented with 10% fetal bovine serum (FBS, Thermo Scientific). The cells were incubated at 37 °C in a humidified atmosphere of 5% CO_2 and 95% air with the growth medium changed twice every week. Cells seeding was done by removing the medium and adding 2 ml Trypsin (0.25% (w/v))-EDTA (0.53 mM) (Thermo Scientific) to the flask, then observing cells under microscope until cell layer is dispersed. Finally 6 ml medium was added and incubated cultures at 37°C.

3.6. Cytotoxic Effect of Heat at Different Temperature

Hyperthermic treatment of cultured cells was performed by heating HeLa cell pellet at various temperatures (38, 42, 55, and 68°C) for 10 min by direct immersion in a temperature-controlled water bath. Each heated cell was plated in a 60-mm cell culture dish at the concentration of 1×10^4 cells/dish and cultured for 7 days. The number of viable cell was evaluated by the trypan blue dye exclusion method using a hemocytometer and was counted on days 1, 3, and 7.

3.7. Cell Viability Assay Using WST-1

The cytotoxicity of Fe_3O_4-APTMS MNPs was measured using the WST-1 assay (ITSBio, Korea). HeLa cells were seeded at a density of 1×10^5 cells/well in 96-well plates and incubated for 24 hr. Fe_3O_4-APTMS with concentration 10, 12, 15, and 17 mg/ml were added into the culture media in the plate. Untreated cells were used as controls. Cells were incubated in a humidified 5% CO_2 at 37 ◦C for 12, 24, and 48 h respectively. In the

end of incubation time, 10 µl WST-1 solution was added to each wall. After 4 h incubation, shake the plate for 1 min and measured the absorbance using a microtiter plate reader (Molecular Device, USA) at 450 nm. Percentage cell viability was calculated by

$$Cell\ viability = \frac{mean\ test\ wells}{mean\ control\ wells} \times 100\% \tag{3.3}$$

3.8. Cell Labeling Using FITC

Fe_3O_4-APTMS MNPs were dispersed in 2 mL of ethanol, and to this solution was added 0.1 mL FITC solution (1 mg/mL in DMSO). After shaking for 12 h in dark, FITC-conjugated Fe_3O_4-APTMS was obtained by washing with ethanol and water and finally dispersed in water. Subsequently, 1ml of FITC- conjugated Fe_3O_4-APTMS (1 mg/ml) was added to HeLa cells (1×10^5 cells/ml), which were pre-cultured on a 12 well plate for 24 h at 37°C. After 24 h exposure, the growth media was removed and the cells were washed with PBS. Then, the cells were re-incubated with a PBS solution of 3.7% formaldehydethe. FITC- conjugated Fe_3O_4-APTMS and cell nucleus were monitored using fluorescence microscope.

3.9. Loss Power Density Evaluation

The energy dissipation of MNPs in an alternating magnetic field is described as [90]

$$P = \pi\mu_0\chi_0 H_0^2 f \frac{\omega\tau}{1+\omega\tau} \tag{3.4}$$

the frequency of alternating magnetic field; and τ is the effective relaxation time given by

$$\frac{1}{\tau} = \frac{1}{\tau_b} + \frac{1}{\tau_N} \tag{3.5}$$

where τ_N and τ_B are Néel relaxation and the Brownian relaxation time, respectively. In

case of MNPs disperse in agar gel (or in living tissue), Brownian relaxation is neglected because it is ~10^3 times larger than the Neel relaxation time, that has large viscosity [35], where τ_N equals

$$\tau_N = \frac{2\sqrt{\kappa V_M / kT}}{\sqrt{\pi}\,\tau_0\, exp(\kappa V_M / kT} \tag{3.6}$$

and V_M written as

$$V_M = \frac{\pi D^3}{6} \tag{3.7}$$

The equilibrium susceptibility χ_0 expressed as [92]

$$\chi_0 = \chi_i \frac{3}{\xi}\left(coth\,\xi - \frac{1}{\xi} \right) \tag{3.8}$$

where $\xi = \mu_0 M_d H V_M / kT$; $M_d = M_s / \phi$; $H = H_0 cos 2\pi f t$; $\chi_i = \mu_0 \phi M_d^2 V_M / 3kT$

Given the extrinsic (i.e., shape, diameter) and intrinsic (i.e., magnetization) properties of the particles and the intensity value of the exciting magnetic field (Table 3-1), a MATLAB procedure then was developed to estimate the effective power density (W/m^3).

Table 3-1. Numerical values of variables and parameters of the loss power density

Name	Variable	Unit	Dimensional
Fe_3O_4 MNPs size	D	m	1.45×10^{-8}
Ligand thickness	δ	m	1×10^{-9}
Permeability of free space	μ_0	T.m/A	$4\pi \times 10^{-7}$
Saturation magnetization	M_s	Am^2/kg	38.4
Volume fraction of MNPs	ϕ	-	0.0099 (10 mg/ml) 0.0119 (12 mg/ml) 0.0148 (15 mg/ml) 0.0167 (17 mg/ml)
Boltzmann constant	k	J/K	1.38×10^{-23}
Anisotropy constant	κ	J/m^3	9×10^3 [92]
Initial temperature	T	K	293

Average relaxation time	τ_0	s	10^{-9} [92]
Time	t	s	1200
Magnetic field	H_0	kA/m	1.12×10^4
Frequency	f	Hz	1.54×10^5

3.10. Computer-Based Model of Heat Transfer in Agar Tissues

By using COMSOL Multiphysics ver 3.5 (Heat Transfer Module), we intended to compute the spatial temperature distribution within the tissues. For our problem, the temperatures are dependent on time and there is no fluid flow. The only mode of heat transfer is by conduction. So the problem is a transient conduction problem with no convection, the governing equation that needs to be solved is

$$\rho C_p \frac{dT}{dt} - \nabla(\kappa \nabla T) = Q \qquad (3.6)$$

where ρ is the density (kg/m^3), C_p the molar specific heat at constant pressure (J/kg/^{o}C), T the temperature (^{o}C), t the time (s), κ the thermal conductivity (W/m/^{o}C), ∇ means Laplacian, and Q the heat source (W/m^3). The estimated loss power density value was then put as heat source inside the tumor mass and the resulting temperature rise around the tissue.

The 3D symmetry model consists of polystyrene cells culture dish with 1 mm wall thick, homogenous agar tissue layer 5 mm thick and Fe_3O_4-APTMS MNPs which were located in the center of dish and in the bottom side before agar tissue layer (Figure 3-4). Fe_3O_4-APTMS MNPs which had been concentrated using magnet were modeled as sphere with 0.5 mm thick and diameter sizes are depend of the amount of concentrations (Table 3-2). The physical properties of the materials are presented in Table 3-3.

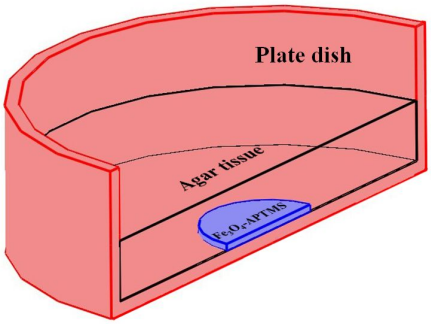

Figure 3-4. A 3D symmetry half model of agar tissue in the presence of MNPs

Table 3-2. Diameter of MNPs regions based on concentration

Fe_3O_4-APTMS concentration (mg/ml)	diameter region (mm)
10	8.2
12	10.0
15	11.0
17	12.6

Table 3-3. Physical properties of material applied in computer based simulation

Physical properties	Fe_3O_4-APTMS [92]	Agar tissue [36]	Polystyrene [97]
Heat capacity (J/kg.C^o)	670	4183	1300
Thermal conductivity (W/m. C^o)	6	0.6072	0.08

The investigation was focused on the upper surface of agar, following our experiment, where the verification only can be done on the upper surface of agar. Initial temperature was set at 20^{o}C. All surfaces of the plate dishes were adjusted using initial temperature except the bottom surface. Moreover, the thermal insulation was applied on the agar surface and the surfaces along the symmetry line. The heat source was addressed on the

MNPs regions. In this study, the analysis time was set in 1200 second. The models were constructed using a mesh consisting of tetrahedral element. The total number of the tetrahedral element automatically and optimally generated by COMSOL. The UMFPACK direct solver and adequate conditions needed for each calculation was automatically selected by COMSOL.

3.11. Numerical investigation

A numerical model is constructed to calculate the heat diffusion characteristic of the heat source dispersing MNPs in agar tissue are shown in Figure 3-5. The heat source (radius of a) in alternating magnetic field is assumed to dissipate constant power. And also, the Fe_3O_4/APTMS-dispersed spherical heat source is assumed to be surrounded by particle free agar gel ($a < r < b$). Additionally, we have assumed the above spherical composite (Fe_3O_4/APTMS-dispresed agar gel and Fe_3O_4/APTMS-free agar gel) sphere is surrounded by a layer of air ($b < r < R$) [34].

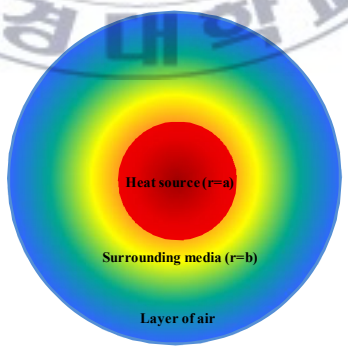

Figure 3-5. Schematic diagram of numerical model

The radius of b and effective radius, R are calculated by the following equation:

$$r = 3 \times \frac{Volume}{Surface\ area} \tag{3.7}$$

The governing equations for the x-z plane heat diffusion in agar surface are as follows:

$$\rho c \frac{\partial T_1}{\partial t} = \frac{1}{r^2}\frac{\partial}{\partial r}\left(kr^2 \frac{\partial T_1}{\partial t} \right) + Q\,(0 < r < a) \tag{3.8}$$

$$\rho c \frac{\partial T_2}{\partial t} = \frac{1}{r^2}\frac{\partial}{\partial r}\left(kr^2 \frac{\partial T_2}{\partial t} \right) + Q\,(a < r < b) \tag{3.9}$$

$$\rho c \frac{\partial T_3}{\partial t} = \frac{1}{r^2}\frac{\partial}{\partial r}\left(kr^2 \frac{\partial T_3}{\partial t} \right) + Q\,(b < r < R) \tag{3.10}$$

where ρ is the density of mass, c the specific heat, k the heat conductivity, r the distance from the center of heat source (sphere dispersing MNP), T the temperature (T_1 is the temperature in the heat source, T_2 the temperature in the surrounding media and T_3 is the temperature in the later of air) and Q the heat evolution.

The initial and boundary condition are

$$T_1(r,0) = T_2(r,0) = T_3(r,0) = T_e \tag{3.11}$$

$$\left(\frac{\partial T_1}{\partial_r} \right) = 0 \tag{3.12}$$

$$\left(\frac{\partial T_1}{\partial_r} \right) = \left(\frac{\partial T_2}{\partial_r} \right) (r = a) \tag{3.13}$$

$$\left(\frac{\partial T_2}{\partial_r} \right) = \left(\frac{\partial T_3}{\partial_r} \right) (r = b) \tag{3.14}$$

where T_e is the initial temperature 20°C. The ρ, c and k of Fe_3O_4/APTMS-dispresed agar gel.

Chapter 4

Results and Discussion

4.1. Fe_3O_4 MNPs Crystal Characterization

The crystal structure Fe_3O_4 MNPs were characterized through X-ray diffraction (XRD). XRD has been in use in two main areas, for the fingerprint characterization of crystalline materials and the determination of their structure. Each crystalline solid has its unique characteristic [98]. Figure 4-1. represents the XRD pattern of Fe_3O_4 at 2θ = 30.3, 35.5, 36.5 42.5, 57.0, 62.2, and 73.4 which correspond to 220, 311, 400, 511, 440, and 533 Bragg reflection. These peaks are consistent with the standard pattern of Fe_3O_4 (JCPDS 79-0418) with a cubic inverse spinel structure.

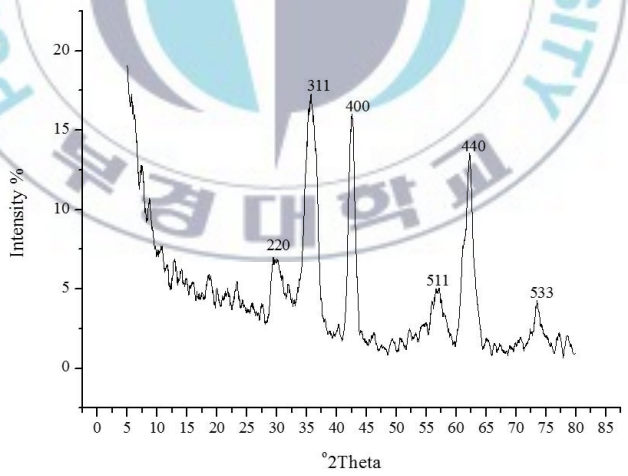

Figure 4-1. X-ray diffraction pattern of Fe_3O_4-oleic acid NPs

4.2. Surface Modification of Fe_3O_4 MNPs via Ligand Exchange

As was established previously, Fe_3O_4 in the presence of surfactants such as oleic acid are stable in nonpolar solvents (such as hexane) and capped with nonpolar endgroups on their surface [99]. Therefore, to increase the biocompatibility of MNPs, ligand exchange

was needed for tuning the surface properties into hydrophilic. Alkylsilanes was the best candidate for its effectiveness and simplicity to conduct exchange of hydrophobic ligands on Fe_3O_4 MNPs and present stabilization of nanoparticles [95].

The ligand exchange in the chemical groups present in the nanoparticles was verified using FT-IR. The typical of FT-IR spectra of Fe_3O_4 MNPs are shown in Figure 4-2(A). The C=O at 1711 cm^{-1}, the C-H stretch at 2911 cm^{-1}, and the CH_2/CH_3 bending at 1464 cm^{-1} are evidence of oleic acid-coated Fe_3O_4 NPs. The FT-IR spectra of Fe_3O_4-APTMS, see Figure 4-2(B), showed the peaks around 1638 cm^{-1} ascribed to the $–NH_2$ terminal of APTMS, the CH_2 bending were found at 1450 cm^{-1}, the C-H stretch at 2921 cm^{-1}, the Si-O-Si bridges were seen at 1098 cm^{-1}, and the Si-O bound at 900cm^{-1}. The absent of oleic acid peaks and replaced by silane peaks in Fe_3O_4 MNPs indicates that ligand exchange was successfully done.

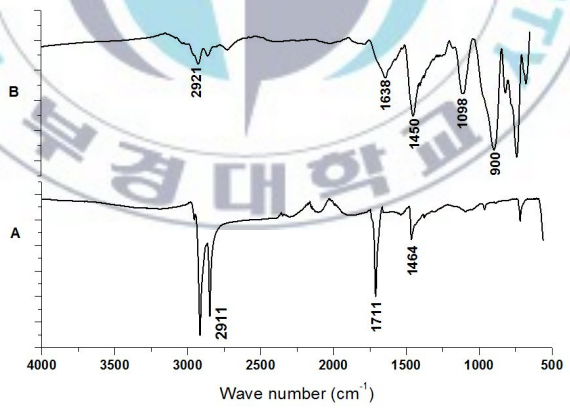

Figure 4-2. The FT-IR spectrums of Fe_3O_4-oleic acid (A) and Fe_3O_4-APTMS (B).

4.3. TEM Image Characterization

Imaging and analytical characterization of nanoparticle by Transmission Electron Microscopy (TEM) is commonly performed to assess shape, size, morphology, and elemental distributions. The outstanding resolution achieved by TEM is an excellent fit

for these challenging studies. According to TEM, as illustrated in Figure 4-3(A), the thermo decomposition method resulted Fe_3O_4-oleic acid MNPs with a number mean diameter of 14.5 nm and a geometric deviation of 0.33 by fitting the diameters to a number averaged lognormal distribution [100]:

$$n_n(D_p) = \frac{1}{\sqrt{2\pi} D_p \ln \sigma_g} \exp\left(- \frac{\ln^2 (D_p / D_{pg}}{2 \ln^2 \sigma_g} \right) \quad (4.1)$$

Lognormal distribution was chosen to fit the particle size distribution from TEM, where $n_n(D_p)$ is the probability density for particles having diameter D_p, D_{pg} is the number mean diameter of the distribution, and $ln\ \sigma_g$ is the geometric deviation of the distribution.

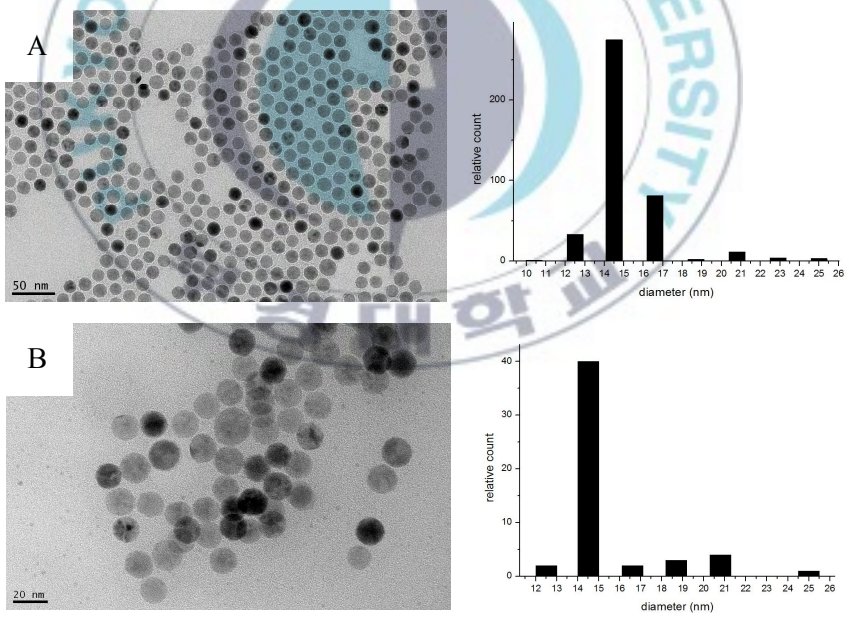

Figure 4-3. TEM images and particle size distributions of Fe_3O_4-oleic acid (A) and Fe_3O_4-APTMS (B)

Figure 4-3B shows a representative TEM image of the nanoparticles after ligand exchange with APTMS. The resulting particles have a number mean diameter of 14.5 nm

and a geometric deviation of 0.36. These results suggested that ligand exchange process doesn't have significant effect to change the particle size, both Fe_3O_4-oleic acid and Fe_3O_4-APTMS MNPs had close particle size. And it also can be seen that particles were spherical shape with a narrow size distribution and uniform physico-chemical properties.

4.4. Magnetic Properties

The magnetization values of nanoparticles were measured by Superconducting Quantum Interference Device (SQUID). Figure 4-4 shows the magnetic curves as function of applied field at 300K. The saturated magnetization of Fe_3O_4-APTMS MNPs was about 38.4 emu/g, which was lower than those of Fe_3O_4-oleic acid MNPs was about 57 emu/g. Moreover, the remanence (M_r) and coercivity (H_c) were close to zero, exhibiting the characteristic of supramagnetic. Decrease of magnetization related to high magnetocrystalline anisotropy of Fe_3O_4 in the presence of APTMS which formed polymerized multilayers, suppressing a tendency to destabilization of magnetic ordering.

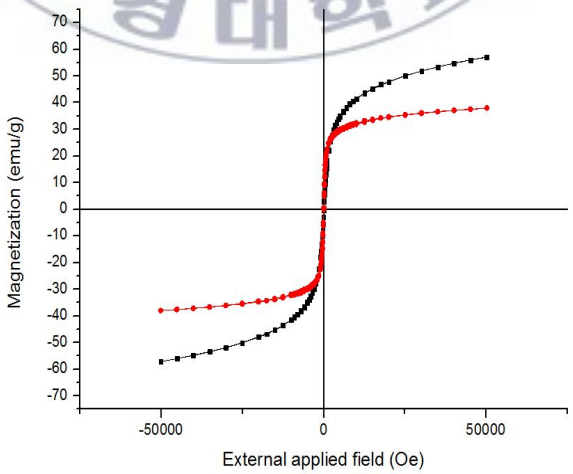

Figure 4-4. Magnetic hysteresis for Fe_3O_4-oleic acid (■) and Fe_3O_4-APTMS (●), measured at room temperature

4.5. Increase of Temperature on Agar Tissue Surface containing Fe_3O_4-APTMS MNPs When Exposed to The Magnetic Field

Figure 4-5 summarizes the results of our *in vitro* experiment using 1.2 % agar in a polystyrene cells culture dish containing 10, 12, 15, and 17 mg Fe_3O_4-APTMS/ml When exposed to the magnetic field, the temperature increased sharply. The upper surface temperatures of agar tissue, which the region of 5 mm from a center of the MNPs sphere were observed have *Tc* (maximum self-controlled temperature) of 34.5 ^oC, 38.6 ^oC, 49.1 ^oC, and 61.4^oC, respectively within 20 min. These results were compared with *Tc* for Fe_3O_4-APTMS MNPs in the absence of agar tissue, it were 38.4 ^oC, 42.6 ^oC, 55.1 ^oC, and 68.1^oC, respectively. The temperature decreases proved the heat diffusion process in the tissue.

In order to illustrate SAR as a function of MNPs content, their values are plotted in Figure 4-6. Since the nanoparticles are the only heating sources present in the agar tissue, the SAR distribution can be used as an index for the particle concentration in the gel. The temperature curve at upper surface 5 mm away from the center of the MNPs are used to determine the SAR values based on Eq. (3.1) For magnetic field strengths 130 Oe, the SAR value was sensitive to the concentration of Fe_3O_4- APTMS MNPs. 10 mg /ml corresponds to an applied heat dose of 14.9 W/g_{tissue}. Similarly, 12, 15, and 17 mg/ml corresponds to an applied heat dose of 15.9, 19.9, 25.0 W/g_{tissue}, respectively. Herein, we got some insight into the observed variation value of SAR, it enables good automatic temperature control throughout the tumor as a result of the self-regulating nature of the thermosensitive materials. Moreover, the heat dose required to increase the temperature of an in vitro tissue phantom model up to 50^oC is in the range 19-25 W/g_{tissue}.

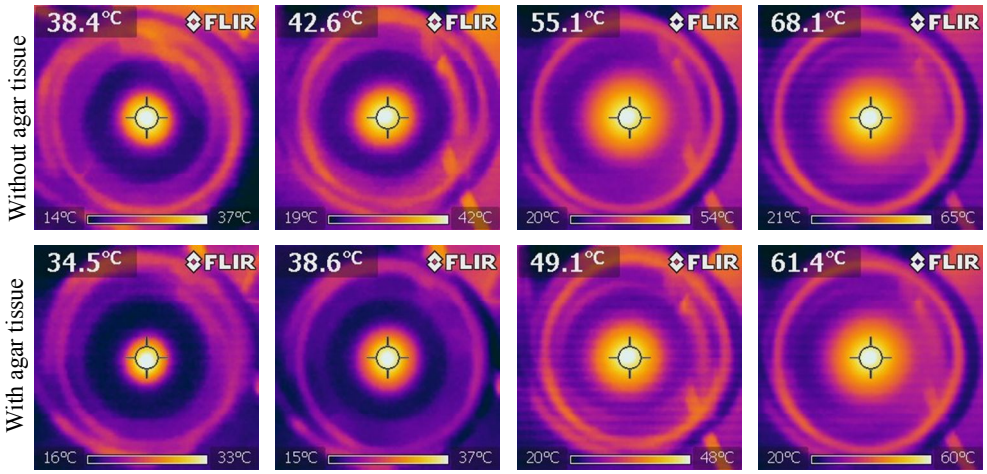

Figure 4-5. Thermal response on agar surfaces. Temperature was observed from above using IR camera. To show the heat transfer process in agar gel, temperature was measured with and without agar. Increase of temperatures was found to be proportional to the quantity of the particles.

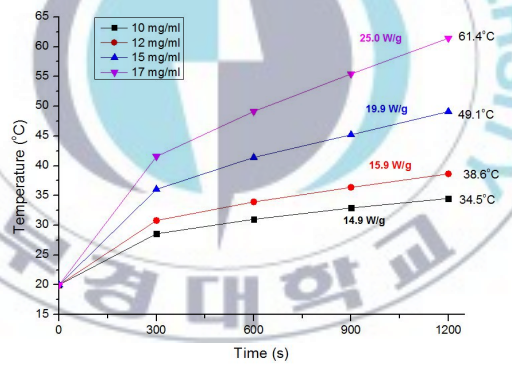

Figure 4-6. Heat doses and time-dependent temperature increases in agar tissue based on experiment, observed at the upper surface 5 mm from Fe_3O_4-APTMS MNPs sphere.

4.6. Loss Power Density of MNPs and Temperature Prediction

The loss power density (P) values of MNPs with four different concentrations are shown in Table 4-1. These values were then put as heat source (Q) at Eq. (3.6). Temperature prediction using COMSOL was done for each concentration of MNPs, where particle was distributed in one spherical region with specific diameter size.

Tabel 4-1. The SAR and loss power density value for different concentrations

Concentration of Fe_3O_4-APTMS (mg/ml)	SAR (W/g_{tissue})	Loss power density, P (W/m^3)
10	14.9	4.86×10^6
12	15.9	5.86×10^6
15	19.9	7.56×10^6
17	25.0	8.69×10^6

The time-dependent changes in the temperature of Fe_3O_4-APTMS MNPs heating are shown in Figure 4-7. The achieved temperature within 20 min for samples with concentration of 10, 12, 15, and 17 mg/ml were 38.0 °C, 42.8 °C, 55.3 °C, and 68.2 °C, respectively. Our simulation showed close agreement to our experiment in Fig. 4-5. Further, the simulation results showed that in the superparamagnetic behavior, the concentration of the particles is much more significant in determining the amount of generated heat, as opposed to the parameters of field amplitude and frequency.

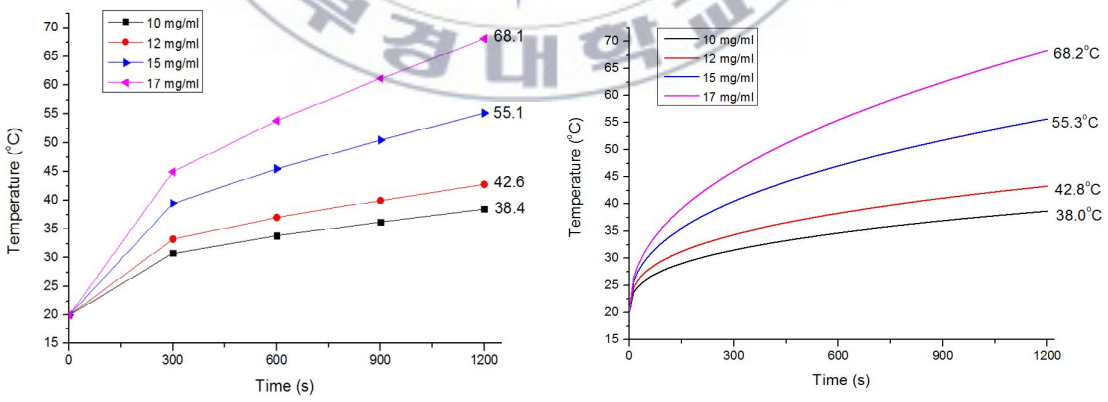

Figure 4-7. The time-dependent change in the temperature of Fe_3O_4-APTMS MNPs based on experiment (left) and obtained from computer simulation (right).

4.7. Simulation of thermal gradient *in vitro* agar tissue phantom

3D thermal gradient simulations in agar tissue with Fe_3O_4-APTMS MNPs as heat source are shown in Figure 4-8. The temperature differences and curves of achieved temperature in the x-z plane of the upper surface of agar (5 mm distance from it using a concentration of MNPs) are shown in Figure 4-9. When concentrations of sample were 10, 12, 15, and 17 mg/ml , the temperature at the centre of tissue increased to 34.0 °C, 38.1 °C, 48.8 °C, and 61.0 °C, respectively. These simulation data were quite comparable to actual experimental data (Figure 4-6), indicating the validity of the COMSOL Multiphysics simulation results. In order to obtain temperature higher than of 42 °C, concentration of Fe_3O_4-APTMS MNPs of 15 mg/ml has been chosen.

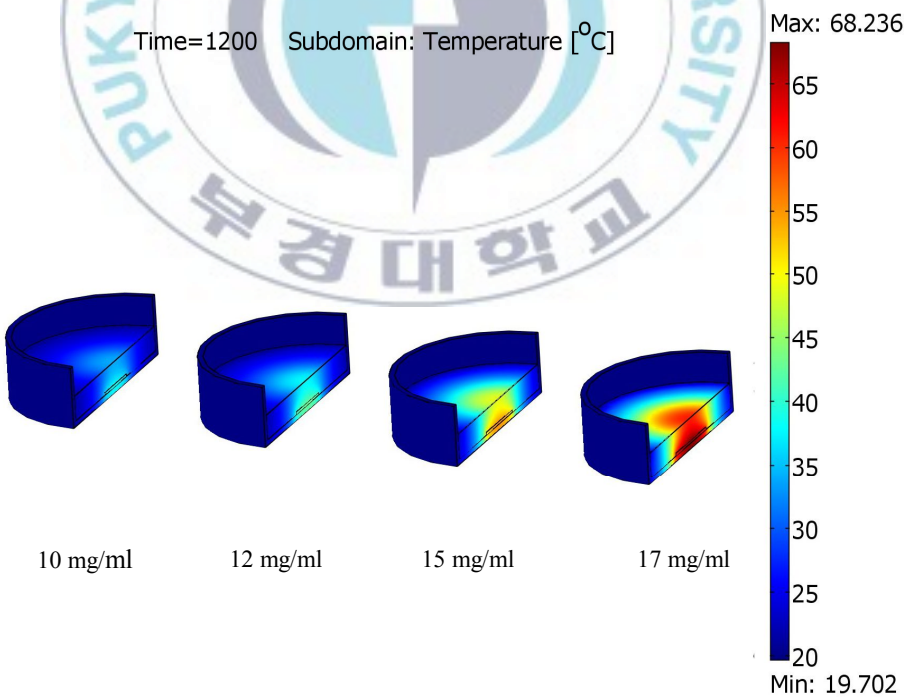

Figure 4-8. Simulation of thermal gradient in agar gels (1.2%), which was heated with four different concentration of Fe_3O_4-APTMS MNPs for 20 min.

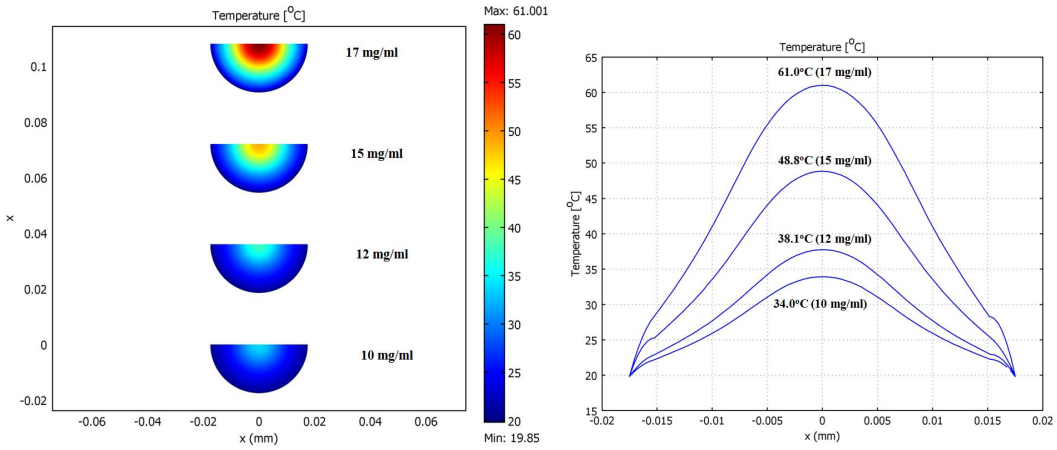

Figure 4-9. Heat distributions in the upper surface of agar observed in x-z plane (left). Curves represent temperature along a line parallel to the x-axis for different obliqueness angles in the x-z-plane (right).

4.8. Cytotoxic Effect of Heat

The number of viable cancer cells 1, 3, and 7 days after exposure to four different temperatures is shown in Figure 4-10. The growth curves indicated that HeLa cells were relatively sensitive to heating temperature during 10 minutes exposure time. When cells were heated at temperature of 38°C, the number of cells growth decreased significantly compared with control which was incubated at 37°C.

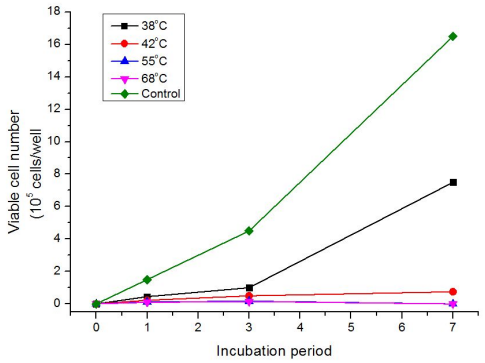

Figure 4-10. Cytotoxic effect of heat treating in HeLa cell. After 10 min exposure to various temperatures (38°C, 42°C, 55°C, and 68°C), the numbers of viable cells were counted at 1, 3, and 7 days after incubation. The values and bars are the mean and SD of three independent experiments.

Further, our results confirmed that exposure to temperature of 42°C can induce obvious cellular damage but it still allowing cell grow after 7 days. This result is agreed with previous findings [101-102]. Moreover, exposures to temperatures of 55 and 68°C were more than enough to kill cells, there were no viable cell found even after incubation for one day.

4.9. Evaluation of *In vitro* Cell Viability

The potential toxicity of Fe_3O_4-APTMS MNPs to HeLa cell was demonstrated by WST-1 cytotoxicity assay. This assay is based on the cleavage of the tetrazolium salt to water soluble formazan by succinate-tetrazolium reductanse system which belongs to the respiratory chain of the mithocondria and active only in the viable cells [103]. Therefore, the amount of the formazan dye is directly proportional to the number of living cell. The presence of cell viability was examined after cells were incubated in various periods 12, 24, and 48 h. WST-1 assay indicated viability greater than 50% for all sample and were shown stable for each incubation period, see Figure 4-11. It means particles didn't have significant effect on cell viability and was categorized as not toxic. The relationship to concentration indicates that, at the highest concentration, the cells died more quickly, and they died more slowly with decreasing concentration.

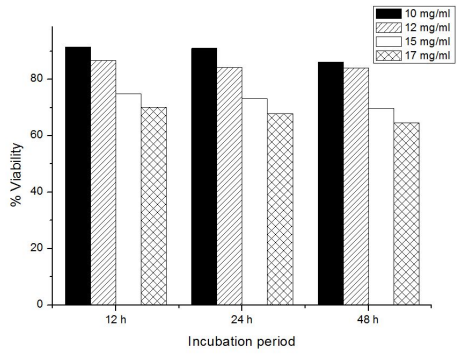

Figure 4-11. Percent viability of HeLa cell in the presence of Fe_3O_4-APTMS

4.10. Cellular uptake of FITC-labeled Fe_3O_4-APMTS

Confocal fluorescence scanning microscope (Leica Microsystem, Germany) was used to observe the uptake of FITC-labeled Fe_3O_4-APTMS MNPs in HeLa cells after 12 h incubation is shown in Figure 4-12. As shown, the fluorescence (green) areas, after 12 h exposure, the FITC-labeled Fe_3O_4-APTMS MNPs particles can present in cytoplasm. Meanwhile, the HeLa cells treated by these nanoprticles still remained large, spindle-shaped, which reveals a nice biocompatibility of the synthesized Fe_3O_4-APTMS MNPs.

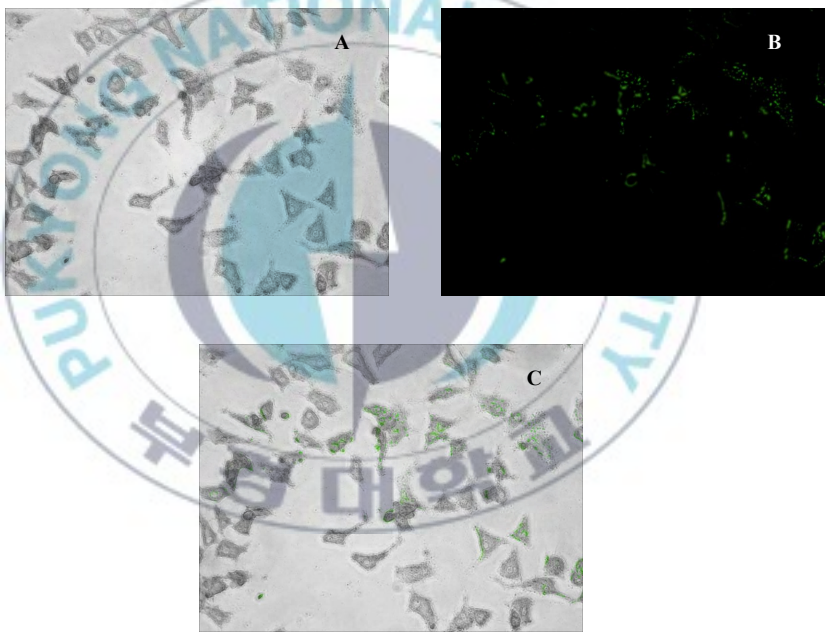

Figure 4-12. Microscope images of HeLa cells after incubated with FITC-labeled Fe_3O_4-APTMS MNPs for 12 h. (A) is bright field represents phase contrast , (B) is green channel of fluorescence, and (C) is overlay.

4.11. Discussion

We have developed a hyperthermia treatment protocol that makes use of Fe_3O_4-APTMS MNPs designed to produce heat for effective magnetic hyperthermia therapy. As reported earlier by J. Oleson and W. Andra [104-105], the temperature distribution is of

great importance in determining how successful the treatment is, that is, how much of the tumor is heated to therapeutic temperatures, and how much of the surrounding normal tissue is damaged by the heat. Since agar gel is equivalent as heat-sensitive gels for phantom measurements and treatment verification purposes [106]. Agar tissue was used as the representative tumor to examine the amount of Fe_3O_4-APTMS MNPs that provides a heat dose. According to our experiment result, for local magnetic hyperthermia using Fe_3O_4-APTMS MNPs, concentration of 12 mg/ml and SAR value 15.9 W/g_{tissue} can be chosen. But for large tumor, may be treated by applying heat dose of 19.9 W/g_{tissue}, which resulted from concentration of 15 mg/ml.

Before using the software COMSOL for present heat simulation, we confirmed its reliability by comparing the data obtained by using it with the experimental data. The value of the loss power density is the basic input parameter for COMSOL. The results showed that in the superparamagnetic behavior, the concentration of the particles is much more significant in determining the amount of generated heat, as opposed to the parameters of field amplitude and frequency. However, in order to obtain the same size for the optimum temperature region for the same concentration of nanoparticles as in the superparamagnetic regime, we observed that the field amplitude and frequency must be significantly increased [107]. By entering value of magnetic field of 130 Oe (at 154 kHz) into COMSOL, the simulated temperature at the center of sphere MNPs (Fig. 6) were observed to be well correlated with those detected experimentally (Fig. 4B). This result indicates that COMSOL can be used in future studies for simulation of temperatures *in vivo*.

The transfer of thermal energy in living tissues is a complex process which involves both metabolic heat and blood flow. For example, the blood flow within the tissue is

increased by thermoregulation in order to remove the heat supply [108-109], therefore the cooling effect of blood flow should also be taken into consideration in a clinical setting [110-111]. It is true that the presence of blood flow acts as a heat radiator and disrupts heating the tumor, we eliminate blood flow issue from our estimation since this obstacle may be overcome by employing a surgical technique known as Pringle's manoeuvre [112] which temporally occludes hepatic vascular inflow. The efficacy of Pringle's manoeuvre in reducing heat loss has been clinically shown in radio-frequency ablation treatment [113]. We therefore focused only on static thermal diffusion loss to surrounding tissues as a heat loss factor.

In order, to define the required temperature for cancer cell killing, we demonstrated the influence of heating treatment with the number of cells growth. Since heat sensitivity of clinical cancers is known to be variable, we used cell pellet to represent the hard tumor tissue following the previous methods [38, 114] and it was found that HeLa cells are relatively sensitive to heating temperature. We applied the treatment time at 10 min, since long irradiation of AC magnetic field to living body tissue causes adverse events [115]. Our results (Fig. 8) demonstrated that maintaining a temperature of 42^{o}C for 10 min was insufficient and resulted in the reproliferation of cancer cells, while a temperature of 55^{o}C maintained for 10 min resulted in complete cell death regardless of the heat sensitivity of each cell type.

Cytotoxicity measurements were originally designed for rapid and inexpensive analysis of soluble pharmaceuticals. They are also useful in the initial development of novel nanoparticle formulations. As these results demonstrate, the particular cytotoxicity assay selected could produce erroneous findings due to nanoparticle-assay interference, and thus careful experimental design is required to detect potential interactions. In this

study, WST-1 assays were used to quantify cellular viability, which in contrast to the formazan product generated in the MTT assay [116]. Cell viability using MTT assay showed the formazan dye crystals generated by live cells were dissolved in DMSO, we confirmed in our experiments that Fe_3O_4-APTMS MNPs were soluble in DMSO and showing interferences caused by these particles. Keeping in mind these interactions, we assessed MNPs potential cytotoxicity by use of the WST-1 assay; the WST-1 has been validated in various *in vitro* cel viability assays using such particles [117-118]. Here, we also examined the feasibility of using these MNPs as an intracellular delivery carrier. FITC, an extensively used fluorescent marker [119-120] was used as to label nanoparticles. The results clearly demonstrated that these Fe_3O_4-APTMS MNPs could serve as an efficient absorptive endocytosis into the cell cytoplasm.

Conclusions

In this study, we have investigated the heat diffusion characteristics of MNPs dispersed in agar tissue using simulation and experimental measurement for various concentrations. Our results show that by using these models, we can successfully estimate the impact of the particle dose on the efficiency of hyperthermia therapy. It could be thus a good method to evaluate the prospects of the therapy and also to establish an optimum starting dose for magnetic hyperthermia therapy in such a case. Moreover, Fe_3O_4-APTMS MNPs exhibited good magnetic properties, biocompatibility, low cytotoxicity and efficient endocytosis. Thus, based on our obtained results, it can be concluded that Fe_3O_4-APTMS MNPs will have excellent potential as novel magnetic nanoparticles for hyperthermia.

References

1. Cascinu, S., et al., *Locoregional treatments of unresectable liver metastases from colorectal cancer.* Cancer treatment reviews, 1998. **24**(1): p. 3-14.
2. Kumar, C.S.S.R., *Nanomaterials for cancer diagnosis*. 2007: Vch Verlagsgesellschaft Mbh.
3. Zahn, M., *Electromagnetic Field Theory: a problem solving approach*. 1979: Wiley.
4. Jordan, A., et al., *Inductive heating of ferrimagnetic particles and magnetic fluids: physical evaluation of their potential for hyperthermia.* International Journal of Hyperthermia, 1993. **9**(1): p. 51-68.
5. Chou, C.K., *Use of heating rate and specific absorption rate in the hyperthermia clinic.* International Journal of Hyperthermia, 1990. **6**(2): p. 367-370.
6. Batlle, X. and A. Labarta, *Finite-size effects in fine particles: magnetic and transport properties.* Journal of Physics D: Applied Physics, 2002. **35**: p. R15.
7. Tartaj, P., et al., *The preparation of magnetic nanoparticles for applications in biomedicine.* Journal of Physics D: Applied Physics, 2003. **36**: p. R182.
8. Arruebo, M., et al., *Magnetic nanoparticles for drug delivery.* Nano Today, 2007. **2**(3): p. 22-32.
9. Pamme, N. and C. Wilhelm, *Continuous sorting of magnetic cells via on-chip free-flow magnetophoresis.* Lab Chip, 2006. **6**(8): p. 974-980.
10. Wilhelm, C. and F. Gazeau, *Universal cell labelling with anionic magnetic nanoparticles.* Biomaterials, 2008. **29**(22): p. 3161-3174.
11. Tran, N. and T.J. Webster, *Nanotechnology for bone materials.* Wiley

Interdisciplinary Reviews: Nanomedicine and Nanobiotechnology, 2009. **1**(3): p. 336-351.

12. Pareta, R.A., E. Taylor, and T.J. Webster, *Increased osteoblast density in the presence of novel calcium phosphate coated magnetic nanoparticles.* Nanotechnology, 2008. **19**: p. 265101.

13. Bock, N., et al., *A novel route in bone tissue engineering: Magnetic biomimetic scaffolds.* Acta Biomaterialia, 2010. **6**(3): p. 786-796.

14. Dobson, J., *Magnetic nanoparticles for drug delivery.* Drug development research, 2006. **67**(1): p. 55-60.

15. Sun, C., J.S.H. Lee, and M. Zhang, *Magnetic nanoparticles in MR imaging and drug delivery.* Advanced drug delivery reviews, 2008. **60**(11): p. 1252-1265.

16. Veiseh, O., J.W. Gunn, and M. Zhang, *Design and fabrication of magnetic nanoparticles for targeted drug delivery and imaging.* Advanced drug delivery reviews, 2010. **62**(3): p. 284-304.

17. Corot, C., et al., *Recent advances in iron oxide nanocrystal technology for medical imaging.* Advanced drug delivery reviews, 2006. **58**(14): p. 1471-1504.

18. Yang, F., et al., *Superparamagnetic iron oxide nanoparticle-embedded encapsulated microbubbles as dual contrast agents of magnetic resonance and ultrasound imaging.* Biomaterials, 2009. **30**(23-24): p. 3882-3890.

19. Jordan, A., et al., *Magnetic fluid hyperthermia (MFH): Cancer treatment with AC magnetic field induced excitation of biocompatible superparamagnetic nanoparticles.* Journal of Magnetism and Magnetic Materials, 1999. **201**(1-3): p. 413-419.

20. Johannsen, M., et al., *Clinical hyperthermia of prostate cancer using magnetic*

nanoparticles: presentation of a new interstitial technique. International Journal of Hyperthermia, 2005. **21**(7): p. 637-647.

21. Johannsen, M., et al., *Thermotherapy of prostate cancer using magnetic nanoparticles: feasibility, imaging, and three-dimensional temperature distribution.* European urology, 2007. **52**(6): p. 1653-1662.

22. Pankhurst, Q.A., et al., *Applications of magnetic nanoparticles in biomedicine.* Journal of Physics D: Applied Physics, 2003. **36**: p. R167.

23. Cavaliere, R., et al., *Selective heat sensitivity of cancer cells. Biochemical and clinical studies.* Cancer, 1967. **20**(9): p. 1351-1381.

24. Dudar, T.E. and R.K. Jain, *Differential response of normal and tumor microcirculation to hyperthermia.* Cancer Research, 1984. **44**(2): p. 605.

25. Halperin, E.C., C.A. Perez, and L.W. Brady, *Perez and Brady's principles and practice of radiation oncology*. 2008: Lippincott Williams & Wilkins.

26. Hergt, R., et al., *Physical limits of hyperthermia using magnetite fine particles.* Magnetics, IEEE Transactions on, 1998. **34**(5): p. 3745-3754.

27. Ma, M., et al., *Size dependence of specific power absorption of Fe3O4 particles in AC magnetic field.* Journal of Magnetism and Magnetic Materials, 2004. **268**(1-2): p. 33-39.

28. Zhang, L.Y., H.C. Gu, and X.M. Wang, *Magnetite ferrofluid with high specific absorption rate for application in hyperthermia.* Journal of Magnetism and Magnetic Materials, 2007. **311**(1): p. 228-233.

29. Bae, S., et al., *Dependence of Frequency and Magnetic Field on Self-Heating Characteristics of NiFe Nanoparticles for Hyperthermia*, in *Magnetics, IEEE Transactions on*. 2006, IEEE. p. 3566-3568.

30. Gazeau, F., M. Lévy, and C. Wilhelm, *Optimizing magnetic nanoparticle design for nanothermotherapy.* Nanomedicine, 2008. **3**(6): p. 831-844.

31. Gellermann, J., et al., *Noninvasive magnetic resonance thermography of recurrent rectal carcinoma in a 1.5 Tesla hybrid system.* Cancer Research, 2005. **65**(13): p. 5872.

32. Van der Zee, J., *Heating the patient: a promising approach?* Annals of oncology, 2002. **13**(8): p. 1173.

33. Issels, R.D., *Hyperthermia adds to chemotherapy.* European Journal of Cancer, 2008. **44**(17): p. 2546-2554.

34. Suto, M., et al., *Heat diffusion characteristics of magnetite nanoparticles dispersed hydro-gel in alternating magnetic field.* Journal of Magnetism and Magnetic Materials, 2009. **321**(20): p. 3483-3487.

35. Okawa, K., et al., *Heating ability of magnetite nanobeads with various sizes for magnetic hyperthermia at 120; kHz, a noninvasive frequency.* Journal of Applied Physics, 2006. **99**(8): p. 08H102-08H102-3.

36. Veverka, M., et al., *Magnetic heating by cobalt ferrite nanoparticles.* Nanotechnology, 2007. **18**: p. 345704.

37. Salloum, M., et al., *Controlling nanoparticle delivery in magnetic nanoparticle hyperthermia for cancer treatment: Experimental study in agarose gel.* International Journal of Hyperthermia, 2008. **24**(4): p. 337-345.

38. Yamada, K., et al., *Minimally required heat doses for various tumour sizes in induction heating cancer therapy determined by computer simulation using experimental data.* International Journal of Hyperthermia, 2010. **26**(5): p. 465-474.

39. Overgaard, J., *The current and potential role of hyperthermia in radiotherapy.* International Journal of Radiation Oncology* Biology* Physics, 1989. **16**(3): p. 535-549.

40. Streffer, C., D. van Beuningen, and N. Zamboglou, *Cell killing by hyperthermia and radiation in cancer therapy.* Treatment of Radioresistant Cancers, edited by M. Abe, K. Sakamoto and TL Phillips (Elsevier/North Holland Biomedical, Amsterdam), 1979: p. 55-70.

41. Streffer, C., *Hyperthermia and the therapy of malignant tumors.* 1987.

42. Moroz, P., S. Jones, and B. Gray, *Magnetically mediated hyperthermia: current status and future directions.* International Journal of Hyperthermia, 2002. **18**(4): p. 267-284.

43. DeNardo, S.J., et al., *Thermal dosimetry predictive of efficacy of 111In-ChL6 nanoparticle AMF-induced thermoablative therapy for human breast cancer in mice.* Journal of Nuclear Medicine, 2007. **48**(3): p. 437.

44. Dewhirst, M.W., et al., *Hyperthermia.* Kirks Current Veterinary Therapy, 2000. **13**: p. 486-492.

45. DeNardo, S.J., et al., *Development of tumor targeting bioprobes (111In-chimeric L6 monoclonal antibody nanoparticles) for alternating magnetic field cancer therapy.* Clinical cancer research, 2005. **11**(19): p. 7087s.

46. Hoopes, P., et al. *Intratumoral iron oxide nanoparticle hyperthermia and radiation cancer treatment (Invited Paper)[6440-19]*. 2007: International Society for Optical Engineering; 1999.

47. Aslam, M., et al., *Silica encapsulation and magnetic properties of FePt nanoparticles.* Journal of colloid and interface science, 2005. **290**(2): p. 444-449.

48. Iwaki, T., et al., *Preparation of high coercivity magnetic FePt nanoparticles by liquid process.* Journal of Applied Physics, 2003. **94**(10): p. 6807-6811.

49. Kodama, R., *Magnetic nanoparticles.* Journal of Magnetism and Magnetic Materials, 1999. **200**(1-3): p. 359-372.

50. Paulus, P., et al., *Magnetic properties of nanosized transition metal colloids: the influence of noble metal coating.* The European Physical Journal D-Atomic, Molecular, Optical and Plasma Physics, 1999. **9**(1): p. 501-504.

51. van Leeuwen, D.A., et al., *Quenching of magnetic moments by ligand-metal interactions in nanosized magnetic metal clusters.* Physical review letters, 1994. **73**(10): p. 1432-1435.

52. Skumryev, V., et al., *Beating the superparamagnetic limit with exchange bias.* Nature, 2003. **423**(6942): p. 850-853.

53. Tran, N. and T.J. Webster, *Magnetic nanoparticles: biomedical applications and challenges.* Journal of Materials Chemistry, 2010. **20**(40): p. 8760-8767.

54. Bouchard, L.S., et al., *Picomolar sensitivity MRI and photoacoustic imaging of cobalt nanoparticles.* Proceedings of the National Academy of Sciences, 2009. **106**(11): p. 4085.

55. Robinson, I., et al., *Size and shape control for water-soluble magnetic cobalt nanoparticles using polymer ligands.* J. Mater. Chem., 2008. **18**(21): p. 2453-2458.

56. Salgueiriño Maceira, V., et al., *Composite silica spheres with magnetic and luminescent functionalities.* Advanced functional materials, 2006. **16**(4): p. 509-514.

57. Gilchrist, R., et al., *Selective inductive heating of lymph nodes.* Annals of Surgery,

1957. **146**(4): p. 596.

58. Lu, A.H., E.L. Salabas, and F. Schüth, *Magnetic nanoparticles: synthesis, protection, functionalization, and application.* Angewandte Chemie International Edition, 2007. **46**(8): p. 1222-1244.

59. Alexiou, C., et al., *Locoregional cancer treatment with magnetic drug targeting.* Cancer Research, 2000. **60**(23): p. 6641.

60. LaMer, V.K. and R.H. Dinegar, *Theory, production and mechanism of formation of monodispersed hydrosols.* Journal of the American Chemical Society, 1950. **72**(11): p. 4847-4854.

61. Den Ouden, C. and R. Thompson, *Analysis of the formation of monodisperse populations by homogeneous nucleation.* Journal of colloid and interface science, 1991. **143**(1): p. 77-84.

62. Ocaña, M., R. Rodriguez Clemente, and C.J. Serna, *Uniform colloidal particles in solution: Formation mechanisms.* Advanced Materials, 1995. **7**(2): p. 212-216.

63. Sugimoto, T., *Monodispersed particles*. 2001: Elsevier Science.

64. Jun, Y., et al., *Nanoscale size effect of magnetic nanocrystals and their utilization for cancer diagnosis via magnetic resonance imaging.* Journal of the American Chemical Society, 2005. **127**(16): p. 5732-5733.

65. Huh, Y.M., et al., *In vivo magnetic resonance detection of cancer by using multifunctional magnetic nanocrystals.* Journal of the American Chemical Society, 2005. **127**(35): p. 12387-12391.

66. Taboada, E., et al., *Relaxometric and Magnetic Characterization of Ultrasmall Iron Oxide Nanoparticles with High Magnetization. Evaluation as Potential T 1 Magnetic Resonance Imaging Contrast Agents for Molecular Imaging.* Langmuir,

2007. **23**(8): p. 4583-4588.

67. Robinson, D.B., et al., *DNA-functionalized MFe2O4 (M= Fe, Co, or Mn) nanoparticles and their hybridization to DNA-functionalized surfaces.* Langmuir, 2005. **21**(7): p. 3096-3103.

68. Salgueiriño-Maceira, V., L.M. Liz-Marzán, and M. Farle, *Water-Based Ferrofluids from Fe x Pt1-x Nanoparticles Synthesized in Organic Media.* Langmuir, 2004. **20**(16): p. 6946-6950.

69. Lee, S.Y. and M.T. Harris, *Surface modification of magnetic nanoparticles capped by oleic acids: Characterization and colloidal stability in polar solvents.* Journal of colloid and interface science, 2006. **293**(2): p. 401-408.

70. Herranz, F., et al., *A new method for the rapid synthesis of water stable superparamagnetic nanoparticles.* Chemistry–A European Journal, 2008. **14**(30): p. 9126-9130.

71. Jain, T.K., et al., *Iron oxide nanoparticles for sustained delivery of anticancer agents.* Molecular pharmaceutics, 2005. **2**(3): p. 194-205.

72. Qin, J., et al., *A high-performance magnetic resonance imaging T2 contrast agent.* Advanced Materials, 2007. **19**(18): p. 2411.

73. Wang, Y., et al., *"Pulling" Nanoparticles into Water: Phase Transfer of Oleic Acid Stabilized Monodisperse Nanoparticles into Aqueous Solutions of -Cyclodextrin.* Nano Letters, 2003. **3**(11): p. 1555-1559.

74. Zhang, T., et al., *A general approach for transferring hydrophobic nanocrystals into water.* Nano Letters, 2007. **7**(10): p. 3203-3207.

75. Narain, R., et al., *Synthesis of monodisperse biotinylated p (NIPAAm)-coated iron oxide magnetic nanoparticles and their bioconjugation to streptavidin.* Langmuir,

2007. **23**(11): p. 6299-6304.

76. Xie, J., et al., *Controlled PEGylation of monodisperse Fe3O4 nanoparticles for reduced non-specific uptake by macrophage cells.* Advanced Materials, 2007. **19**(20): p. 3163-3166.

77. Gravano, S.M., et al., *Methods for the surface functionalization of Fe2O3 nanoparticles with initiators for atom transfer radical polymerization and the formation of core–shell inorganic–polymer structures.* Journal of Polymer Science Part A: Polymer Chemistry, 2005. **43**(16): p. 3675-3688.

78. Kim, J., et al., *Magnetic fluorescent delivery vehicle using uniform mesoporous silica spheres embedded with monodisperse magnetic and semiconductor nanocrystals.* Journal of the American Chemical Society, 2006. **128**(3): p. 688-689.

79. Frankamp, B.L., et al., *Surface modification using cubic silsesquioxane ligands. Facile synthesis of water-soluble metal oxide nanoparticles.* Chemistry of materials, 2006. **18**(4): p. 956-959.

80. Lu, C.W., et al., *Bifunctional magnetic silica nanoparticles for highly efficient human stem cell labeling.* Nano Letters, 2007. **7**(1): p. 149-154.

81. Wang, L., et al., *Monodispersed core-shell Fe3O4@ Au nanoparticles.* The Journal of Physical Chemistry B, 2005. **109**(46): p. 21593-21601.

82. Wang, L., et al., *Iron oxide–gold core–shell nanoparticles and thin film assembly.* J. Mater. Chem., 2005. **15**(18): p. 1821-1832.

83. Yu, H., et al., *Dumbbell-like bifunctional Au-Fe3O4 nanoparticles.* Nano Letters, 2005. **5**(2): p. 379-382.

84. Hagemaier, D.J., *Fundamentals of eddy current testing*. 1990: American Society

for Nondestructive Testing.

85. Kong, J.A., *Electromagnetic wave theory*. 2002: Higher Education Press.

86. Booker, H.G., *Energy in electromagnetism.* 1982.

87. Thompson, M.T., *Simple models and measurements of magnetically induced heating effects in ferromagnetic fluids.* Magnetics, IEEE Transactions on, 1998. **34**(5): p. 3755-3764.

88. Zavitaev, E., A. Yushkanov, and Y.I. Yalamov, *Absorption of electromagnetic radiation by a cylindrical metal particle.* Technical Physics, 2001. **46**(11): p. 1460-1464.

89. Chen, G., *Nanoscale energy transport and conversion.* 2005, Oxford University Press, New York.

90. Rosensweig, R., *Heating magnetic fluid with alternating magnetic field.* Journal of Magnetism and Magnetic Materials, 2002. **252**: p. 370-374.

91. Shliomis, M., *Magnetic fluids.* Soviet Physics Uspekhi, 1974. **17**: p. 153.

92. Maenosono, S. and S. Saita, *Theoretical assessment of FePt nanoparticles as heating elements for magnetic hyperthermia.* Magnetics, IEEE Transactions on, 2006. **42**(6): p. 1638-1642.

93. Szasz, A., et al., *An energy analysis of extracellular hyperthermia.* Electromagnetic Biology and Medicine, 2003. **22**(2-3): p. 103-115.

94. Park, J., et al., *Ultra-large-scale syntheses of monodisperse nanocrystals.* Nature Materials, 2004. **3**(12): p. 891-895.

95. De Palma, R., et al., *Silane ligand exchange to make hydrophobic superparamagnetic nanoparticles water-dispersible.* Chem. Mater, 2007. **19**(7): p. 1821-1831.

96. Hilger, I., et al., *Heating potential of iron oxides for therapeutic purposes in interventional radiology.* Academic radiology, 2002. **9**(2): p. 198-202.

97. Chen, G., et al., *FTIR spectra, thermal properties, and dispersibility of a polystyrene/montmorillonite nanocomposite.* Macromolecular Chemistry and Physics, 2001. **202**(7): p. 1189-1193.

98. Peng, S. and S. Sun, *Synthesis and characterization of monodisperse hollow Fe3O4 nanoparticles.* Angewandte Chemie International Edition, 2007. **46**(22): p. 4155-4158.

99. Jana, N., C. Earhart, and J. Ying, *Synthesis of water-soluble and functionalized nanoparticles by silica coating.* Chem. Mater, 2007. **19**(21): p. 5074-5082.

100. López-Cruz, A., et al., *Water dispersible iron oxide nanoparticles coated with covalently linked chitosan.* Journal of Materials Chemistry, 2009. **19**(37): p. 6870-6876.

101. Hickey, E.D. and L.A. Weber, *Modulation of heat shock polypeptide synthesis in HeLa cells during hyperthermia and recovery.* Biochemistry, 1982. **21**(7): p. 1513-1521.

102. Ito, A., et al., *Magnetite nanoparticle-loaded anti-HER2 immunoliposomes for combination of antibody therapy with hyperthermia.* Cancer letters, 2004. **212**(2): p. 167.

103. Ishiyama, M., et al., *A combined assay of cell viability and in vitro cytotoxicity with a highly water-soluble tetrazolium salt, neutral red and crystal violet.* Biological & pharmaceutical bulletin, 1996. **19**(11): p. 1518-1520.

104. Oleson, J., et al., *Tumor temperature distributions predict hyperthermia effect.* International Journal of Radiation Oncology* Biology* Physics, 1989. **16**(3): p.

559-570.

105. Andra, W., et al., *Temperature distribution as function of time around a small spherical heat source of local magnetic hyperthermia.* Journal of Magnetism and Magnetic Materials, 1999. **194**(1-3): p. 197-203.

106. Siddiqi, A.K., *Development of tissue-equivalent heat-sensitive gel for the experimental verification of near infrared (nir) laser-mediated cancer detection and therapy.* 2009.

107. Ang, K., S. Venkatraman, and R. Ramanujan, *Magnetic PNIPA hydrogels for hyperthermia applications in cancer therapy.* Materials Science and Engineering: C, 2007. **27**(3): p. 347-351.

108. Lyons, B.E., et al., *Heat loss and blood flow during hyperthermia in normal canine brain I: Empirical study and analysis.* International Journal of Hyperthermia, 1989. **5**(2): p. 225-247.

109. Pennes, H.H., *Analysis of tissue and arterial blood temperatures in the resting human forearm.* Journal of Applied Physiology, 1998. **85**(1): p. 5.

110. Foster, K., H. Kritikos, and H. Schwan, *Effect of surface cooling and blood flow on the microwave heating of tissue.* Biomedical Engineering, IEEE Transactions on, 1978(3): p. 313-316.

111. Liu, K.C. and H.T. Chen, *Analysis for the dual-phase-lag bio-heat transfer during magnetic hyperthermia treatment.* International Journal of Heat and Mass Transfer, 2009. **52**(5-6): p. 1185-1192.

112. Pringle, J.H., *V. Notes on the arrest of hepatic hemorrhage due to trauma.* Annals of Surgery, 1908. **48**(4): p. 541.

113. Percivale, A., et al., *Radiofrequency thermal ablation of hepatocellular*

carcinoma: our five year experience. Ann Ital Chir, 2004. **75**(6): p. 635-642.

114. Shinkai, M., et al., *Intracellular hyperthermia for cancer using magnetite cationic liposomes: in vitro study.* Cancer Science, 1996. **87**(11): p. 1179-1183.

115. Ivkov, R., et al., *Application of high amplitude alternating magnetic fields for heat induction of nanoparticles localized in cancer.* Clinical cancer research, 2005. **11**(19): p. 7093s.

116. L'Azou, B., et al., *In vitro effects of nanoparticles on renal cells.* Particle and Fibre Toxicology, 2008. **5**(1): p. 22.

117. Lu, J., et al., *Solid-state synthesis of monocrystalline iron oxide nanoparticle based ferrofluid suitable for magnetic resonance imaging contrast application.* Nanotechnology, 2006. **17**: p. 5812.

118. Xu, C., et al., *Au–Fe3O4 Dumbbell Nanoparticles as Dual Functional Probes.* Angewandte Chemie International Edition, 2008. **47**(1): p. 173-176.

119. Rossi, L., A. Quach, and Z. Rosenzweig, *Glucose oxidase–magnetite nanoparticle bioconjugate for glucose sensing.* Analytical and bioanalytical chemistry, 2004. **380**(4): p. 606-613.

120. Zhang, Y., et al., *Magnetic nanocomposites of Fe3O4/SiO2-FITC with pH-dependent fluorescence emission.* Chinese Chemical Letters, 2009. **20**(8): p. 969-972.